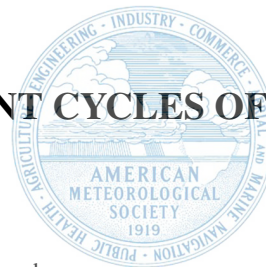# ASYMMETRIES DURING EYEWALL REPLACEMENT CYCLES OF HURRICANE IVAN (2004)

Bruno S. Rojas,[a] Anthony C. Didlake Jr.,[a] Jun A. Zhang,[b]

[a] *Department of Meteorology and Atmospheric Science, The Pennsylvania State University, University Park, Pennsylvania*

[b] *Hurricane Research Division, NOAA/AOML, and Cooperative Institute for Marine and Atmospheric Studies, University of Miami, Miami, Florida*

Corresponding author: Anthony C. Didlake, Jr., didlake@psu.edu

1

ABSTRACT: The physical processes that govern eyewall replacement cycles (ERCs) in tropical cyclones (TCs) are not yet fully understood. In particular, asymmetric structures within the TC inner core have an uncertain role in ERC dynamics. This study analyzes the kinematic and precipitation asymmetric structures during successive ERCs in Hurricane Ivan (2004) using airborne Doppler radar observations. The azimuthal locations of these asymmetries are analyzed relative to the deep-layer (850-200 hPa) environmental wind shear vector. Two ERCs were analyzed at different stages of their evolution. During the concentric eyewall stage of the first ERC, the outer eyewall updrafts were strongest in the left-of-shear half, which also coincided with mesoscale descending inflow (MDI) just radially outward. Enhanced low-level convergence, updrafts, and MDI were collocated in an zone spiraling inward towards the strongest outer eyewall updrafts, suggesting that the vertical velocity asymmetry in the outer eyewall was possibly forced by a stratiform-induced cold pool similar to MDI impacts seen in past TC studies. During the final stage of the second ERC, the outer eyewall (now the singular primary eyewall) experienced an upwind shift in the precipitation and vertical velocity asymmetries. The updraft maximum shifted from the downshear-left quadrant to the downshear-right quadrant, and the precipitation maximum (downwind of the updraft maximum) shifted from left-of-shear to the downshear direction. This shift corroborates previous studies, which hypothesize that at the end of an ERC, the forcing mechanism that drives the eyewall vertical velocity asymmetry transitions from MDI/cold-pool processes to direct interaction with the environmental wind shear.

2

1. Introduction

Eyewall replacement cycles (ERCs) occur often in intense tropical cyclones (TCs) and involve characteristic changes in intensity, storm size, and axisymmetric structure (e.g., Willoughby et al. 1982; Sitkowski et al. 2011). The axisymmetric evolution of ERCs can be divided into three stages: formation of a secondary outer eyewall resulting in two concentric eyewalls, contraction and strengthening of the outer eyewall, and decay of the inner eyewall. The dynamics that govern each stage of an ERC, particularly the role of axisymmetric processes, have been studied in observational (e.g. Sitkowski et al. 2011; Bell et al. 2012; Molinari et al. 2019) and modeling studies (Kepert 2013; Abarca and Montgomery 2015; Wang et al. 2019). Still, the exact physical mechanisms underlying the different ERC stages are not fully known. Asymmetric processes also likely play a role in ERC evolution and impact storm structure and intensity, but their exact role remains uncertain. Such ERC asymmetric processes have not yet been extensively examined in the literature, in part due to the lack of targeted, continuous observations of ERCs by ground-based, airborne, or satellite instruments. The current paper addresses this issue by analyzing asymmetric ERC processes after secondary eyewall formation (SEF) observed by airborne Doppler radar in a well-documented case study.

To examine asymmetric processes in ERCs, one must have an understanding of the major axisymmetric processes that likely govern ERC dynamics. Axisymmmetric processes in secondary eyewall formation (SEF), the beginning stage of an ERC, have been examined extensively in both modeling studies (e.g., Kepert 2013; Wang et al. 2019; Ahern et al. 2021, 2022; Yu et al. 2022; Montgomery and Persing 2021; Persing and Montgomery 2022) and observational studies (e.g., Rozoff et al. 2006; Judt and Chen 2010; Huang et al. 2012; Didlake et al. 2018; Wunsch and Didlake 2018; Vaughan et al. 2020; Fischer et al. 2020; Cha et al. 2021; Razin and Bell 2021; Guimond et al. 2020; Cheung et al. 2023). During the concentric eyewall period, the contraction of the outer eyewall can be explained by axisymmetric dynamics to a large extent. Using the Sawyer-Eliassen equations, Shapiro and Willoughby (1982) showed that the balanced response to an axisymmetric heat source representative of eyewall convection in a vortex includes inward propagation of an axisymmetric tangential wind maximum and updraft maximum. These dynamics would explain contraction of a primary or secondary eyewall. These same axisymmetric processes can also explain the clearing of a precipitation-sparse moat between the two eyewalls, which Houze et al.

3

(2007) described as being analogous to the development of the TC eye. Upper-level divergence over both eyewalls leads to convergence over the moat where air is forced to sink, warm adiabatically, and dry the air. Additionally, Qin et al. (2021) found that microphysical cooling processes forced by the eyewall anvil acted to form an inflow beneath the anvil and further force sinking in the moat.

Hence and Houze (2012) studied satellite-based radar observations of concentric eyewalls. They found that reflectivity values in the upper levels of outer eyewalls resembled those of rainband regions, but the reflectivity values were less than those of inner eyewalls. By contrast, the lower levels of outer eyewalls showed higher reflectivity values and a frequency distribution that more closely resembled the reflectivity characteristics of single eyewalls studied in Hence and Houze (2011). This suggests that the convection processes of outer eyewalls have a mix of inner eyewall and rainband attributes. Hence and Houze (2012) also examined the precipitation asymmetries relative to the deep layer (850-200 hPa) environmental vertical wind shear. The outer eyewall was found to be more resistant to shear asymmetries, with a slight asymmetry favoring precipitation left-of-shear, while the inner eyewall showed a more pronounced asymmetry with precipitation downshear.

Following the concentric eyewall period, the outer eyewall generally continues to contract while the inner eyewall decays. The inner eyewall decay may be explained by an axisymmetric process known as the "barrier effect" where the stronger outer eyewall updrafts divert boundary layer (BL) air upwards, weakening inflow to the inner eyewall (Samsury and Zipser 1995; Houze et al. 2007). Asymmetries do occur in the decaying inner eyewall, but the dynamics of this so-called "relict eyewall" remain uncertain (Sitkowski et al. 2012). Lastly, with a singular eyewall again, the storm can often re-intensify (Sitkowski et al. 2011; Fischer et al. 2020; Shimada et al. 2018) if other environmental conditions remain favorable.

The current study is a follow-up to a previous observational case study, Didlake et al. (2017), which studied asymmetries of Hurricane Gonzalo (2014) during multiple ERCs. During the concentric eyewall stage, they found that the secondary circulation (vertical and radial velocities) of the outer eyewall was strongest in the left-of-shear storm half, downwind of the strongest secondary circulation of the inner eyewall located on the downshear half. This configuration of the secondary circulation asymmetry between the inner and outer eyewalls was consistent with the composite study of Hence and Houze (2012). Subsequently during the inner eyewall decay stage,

4

there was an anticyclonic shift in the outer eyewall secondary circulation asymmetry, with the asymmetry maximum shifting from left-of-shear to the downshear direction. This outer eyewall upwind shift was hypothesized to be a return to the expected precipitation and secondary circulation asymmetry for a single eyewalled storm (Jones 1995; Bender 1997; Frank and Ritchie 1999, 2001; Braun et al. 2006; Rogers et al. 2013; Boehm and Bell 2021). But neither Hence and Houze (2012) nor Didlake et al. (2017) offered a dynamical explanation for the initial outer eyewall asymmetry that was observed. The goals of the current research are to address the physical mechanisms of the outer eyewall asymmetry and examine the ubiquity of the results found in Didlake et al. (2017) by analyzing observations of concentric eyewall evolution in a different case.

This study will use airborne observations to analyze the structure and dynamics of ERCs in the stages after SEF during Hurricane Ivan (2004), which was a long-lived Atlantic Basin TC that underwent multiple, successive ERCs. Ivan completed six eyewall replacements and was undergoing a seventh replacement as it made landfall in Alabama, the largest number of ERCs documented for an Atlantic Basin storm (Sitkowski et al. 2011; Stewart 2004). Fortunately, Hurricane Ivan had numerous reconnaissance missions with periods of nearly continuous coverage with observations of the three-dimensional wind and precipitation during multiple ERCs. National Oceanic and Atmospheric Administration (NOAA) WP-3D (P3) flights into Hurricane Ivan were scheduled to fly with minimal time between flights, with some missions even overlapping, allowing for periods of continuous hurricane coverage longer than single flights would permit. Thus Ivan was chosen for its abundance of ERCs, frequent coverage of the storm by reconnaissance aircraft, and its moderate shear environment permitting the analysis of shear-aligned asymmetries during ERCs. Ivan provides a good comparison to Gonzalo (Didlake et al. 2017) when considering their track and environmental shear variables. Both storms tracked to the north or northwest, and experienced westerly to northwesterly shear during the periods of interest. Differences in intensity were small, ranging from 120-145 kts for Ivan and 105-130 kts for Gonzalo. Differences in shear magnitude were also small, ranging from 5.5-11 m s^{-1} for Ivan and 4.4-6.6 m s^{-1} for Gonzalo. While the Gonzalo kinematic analysis was partly based on Doppler radar observations from the National Aeronautics and Space Administration (NASA) High-Altitude Wind and Rain Airborne Profiler (HIWRAP), the current study uses Doppler radar observations solely from the NOAA P3's tail Doppler radar (TDR) for kinematic analysis, which provided greater spatial coverage (in

5

both horizontal and vertical directions) of the storm's inner core. Additionally, this study utilizes in-situ flight-level measurements, dropsondes, and Lower Fuselage (LF) radar observations. These observations will enable this study to make links between the precipitation asymmetries and underlying dynamics during the ERC. This analysis will help advance our understanding of the dynamical and precipitation processes underlying the eyewall asymmetries during different stages of an ERC. Our findings ultimately may help improve ERC representation in forecast models, leading to better predictions of TC intensity and structure during these events. The paper is structured as follows. Section 2 covers the data and methods used in this study. Section 3 presents an overview of Hurricane Ivan. The results are broken up into Sections 4 and 5, covering the Concentric Eyewall period of 12 Sep, and the Post-Replacement Adjustment period on 14 Sep, respectively. Finally, discussion and conclusions of the results are presented in Section 6.

6

2. Data and Methods

The data for this study were collected from the tail Doppler radar and lower fuselage radar onboard NOAA P3 aircraft. The LF radar is a horizontally scanning C-Band radar that permits observations with wider coverage and high temporal frequency, producing a new scan nearly every minute. The TDR is an X-Band Doppler radar with dual antennas that scan conically around a horizontal axis using the fore/aft scanning technique (Jorgensen et al. 1996). This technique scans a portion of the storm once before passing an area, then scans the same portion again from a different direction after passing the area along the flight path. Given these two independent looks of the wind and given adequate presence of scatterers, the three-dimensional wind vector can then be retrieved. The retrieved TDR wind fields for this study come from the Tropical Cyclone Radar Archive of Doppler Analyses with Recentering (TC-RADAR) dataset (Fischer et al. 2022). In this dataset, the radar observations are first quality-controlled, dealiased, and post-processed using an automated technique (Rogers et al. 2012). The radar projection equations are put into a cost function, along with the constraints of mass continuity and boundary conditions (vertical velocity at the top [18 km] and bottom [0 km] altitudes equal to zero). Then the three-dimensional wind field is retrieved by minimizing the cost function using a variational technique (Gamache 1997; Gao et al. 1999; Reasor et al. 2009).

The retrieved wind field and reflectivity data are solved onto a storm-centered Cartesian coordinate system with 2 km horizontal and 0.5 km vertical grid spacing. The center-finding algorithm used is based on flight-level wind data and is described in Willoughby and Chelmow (1982). The TDR swath coverage extends out to ~65 km from the aircraft for reflectivity and ~45 km for retrieved winds. Table 1 lists the P3 missions and swath times used for this study. We will refer to missions by the unique parts of the mission IDs that denote the date and the P3 (N42 or N43) used for that mission (e.g. 12H refers to the mission flown by N42 on 12 Sep). Additional in-situ flight-level (700 hPa) wind observations from the U.S. Air Force (USAF) C-130 aircraft and the P3s were accessed from the FLIGHT+ dataset (Vigh et al. 2020).

These datasets were all analyzed relative to the deep-layer (850-200 hPa) environmental vertical wind shear vector, which was obtained from the Statistical Hurricane Intensity Prediction Scheme (SHIPS) forecast analysis (DeMaria and Kaplan 1994). The variables used are SHRD and SHTD, which are calculated as the difference between the 850-200 hPa levels in an annulus of 200-800

7

Mission ID	Mission start time	Mission end time	SEF-relative time	ERC	ERC Period
040912I1	2004-09-12 10:42	2004-09-12 15:36	17:34	ERC1	Concentric Eyewall Period
040912H1	2004-09-12 15:51	2004-09-12 20:52	22:46	ERC1	Concentric Eyewall Period
040914H1	2004-09-14 18:25	2004-09-14 23:30	1 day, 2:27	ERC2	Post-Replacement Adjustment
040914I1	2004-09-14 19:52	2004-09-15 03:31	1 day, 5:11	ERC2	Post-Replacement Adjustment

TABLE 1. NOAA P3 missions used in this study. Information includes the mission ID, start and end times (defined as the start of the first leg and end of the last leg) in UTC, time (hh:mm) since the secondary eyewall formation time (based on Wunsch and Didlake (2018)) relative to the mission, and the ERC name and period of focus for each mission. Missions flown by NOAA aircraft N42 are labeled with an "H", and N43 with an "I" in the mission IDs.

km radius as seen in the joint National Centers for Environmental Prediction and National Center for Atmospheric Research (NCEP/NCAR) reanalysis model. SHIPS shear data were validated against shear derived using the Davis et al. (2008) method also on the NCEP/NCAR renanalysis. The two methods yielded shear directions that differed by at most 30° during the times of our analyses, but overall, they produced similar shear magnitudes and directions. Dropsondes used in this study were quality controlled and post-processed at NOAA AOML/HRD (Atlantic Oceanic and Meteorological Laboratory/Hurricane Research Division).

Shear-relative quadrants are identified as follows: downshear-right (DR), downshear-left (DL), upshear-left (UL), and upshear-right (UR). The downshear direction refers to the pointing direction of the shear vector arrow.
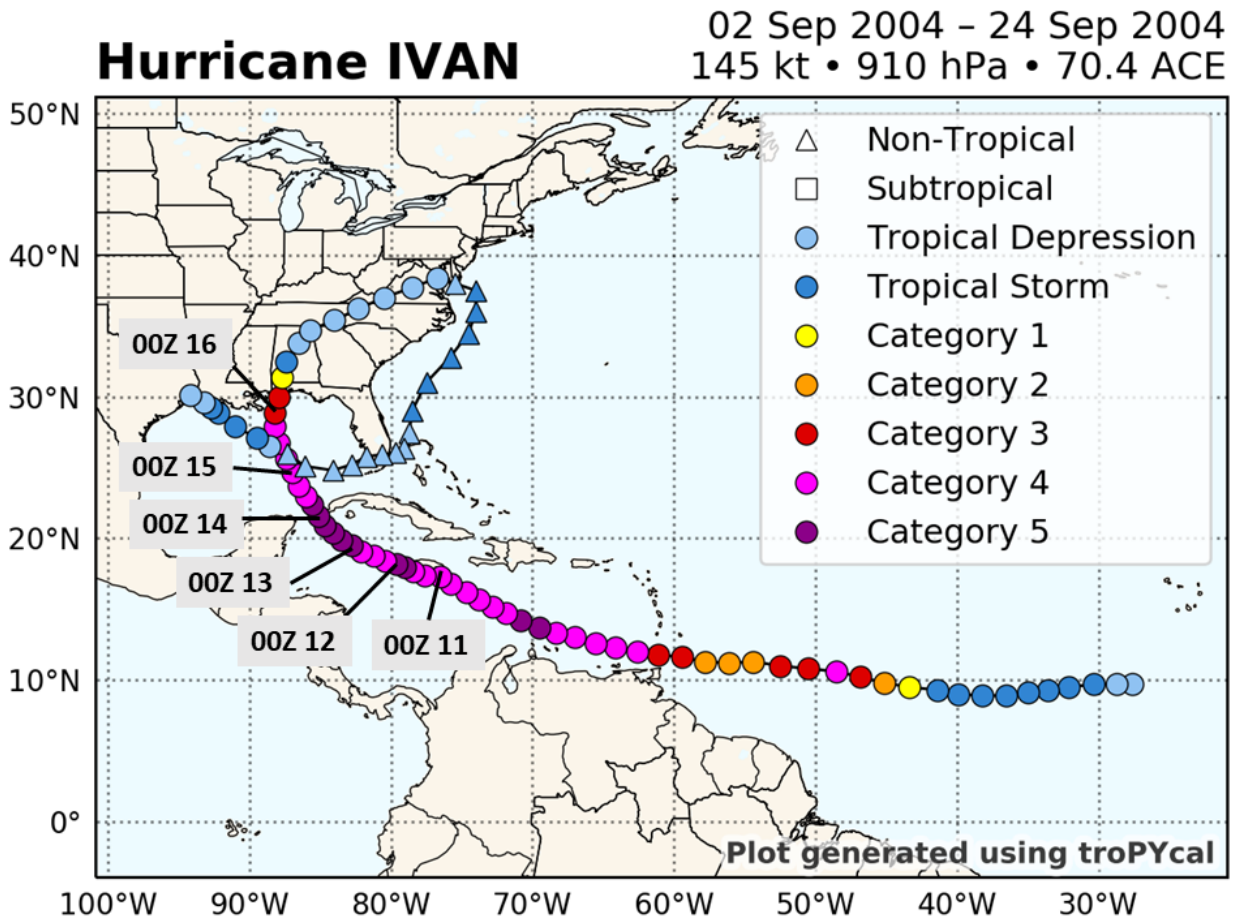
3. Overview of Storm and Data Coverage

Fɪɢ. 1. National Hurricane Center (NHC) Best Track storm centers every 6 hours with dates labeled at 0000 UTC during the period of interest. Shape colors indicate the hurricane category on the Saffir-Simpson hurricane wind scale. Lifetime peak winds, minimum pressure, and storm total Accumulated Cyclone Energy (ACE; Bell et al. (2000)) are labeled in the top right. Plot was created using the Tropycal package (Burg and Lillo 2022).

Figure 1 shows the storm track and intensity category of Hurricane Ivan over its 23-day lifespan. Ivan originated as a westward-tracking Cabo Verde tropical wave. After genesis as a tropical depression around 1800 UTC on 2 Sep, Ivan underwent rapid intensification on 5 Sep, intensifying 50 kts (26 m s^{-1}) in 18 h, reaching maximum sustained winds of 115 kts near 48°W (Stewart 2004). This first peak in intensity was very brief as Ivan encountered dry air and rapidly weakened 20 kts on 6 Sep. On 7 Sep, Ivan began a second period of rapid intensification, reaching 140 kts (Category 5) in the eastern Caribbean on 9 Sep. Figure 2 shows the maximum winds and minimum

9

central pressure from 1200 UTC 10 Sep to 1200 UTC 16 Sep, which covers the investigation period of the current study. During this time, Ivan maintained maximum sustained winds ≥110 kts as it remained over sea surface temperatures greater than 29°C, until it approached land on 16 Sep. Symmetric instability aloft between 300-400 km radius was found by Molinari and Vollaro (2014), and they noted that this may have played a role in prolonging Ivan's intensification. The brief fluctuations of both central minimum sea level pressure and maximum sustained winds are possibly a result of the 4 ERCs Hurricane Ivan experienced from 10 Sep until landfall 16 Sep (Sitkowski et al. 2011).

Sitkowski et al. (2011) described Ivan's impressive succession of ERCs using flight level wind data and microwave imagery. They note that during this period of multiple ERCs not only did the radius of maximum winds (RMW) increase with each ERC, but also the radial extent of hurricane force winds increased with each ERC. Despite Hurricane Ivan's maximum winds remaining within a 25 kt intensity range from 10 to 15 Sep, substantial storm growth was able to occur. In fact, Sitkowski et al. (2011) showed that across all storms in their study, integrated kinetic energy increased an average of 28% and hurricane force wind radius increased by 70% on average following an ERC. Thus, the growth of Ivan's wind field is an expected consequence of the multiple ERCs.

Figure 2 further shows the times of the reconnaissance aircraft missions, as well as the SEF and Maximum Wind Transition (MWT) times for each ERC relevant to this study. The SEF time is defined as the time of the first mission with a secondary wind maximum in the azimuthal mean of the flight level winds. This definition follows the techniques described in Wunsch and Didlake (2018). The MWT time identifies the time where the outer eyewall azimuthal mean flight level winds first exceed the inner eyewall winds, indicating a shift in the radius of maximum winds. Each eyewall maximum wind speed was linearly interpolated between missions to obtain this time as done in Sitkowski et al. (2011).

The ERC occurring primarily on 12 Sep will be called ERC1, and the ERC starting on 13 Sep spanning through 14 Sep will be called ERC2 hereafter. The evolution of the azimuthal averages of flight level winds for ERC1 and ERC2 from both USAF and NOAA P3 aircraft are shown in Figure 3. ERC1 has an archetypal wind progression where the inner eyewall decays with little to no radial contraction and the outer eyewall wind maximum monotonically contracts and intensifies. A marked minimum in wind speed is also present in the moat region during ERC1, maintaining
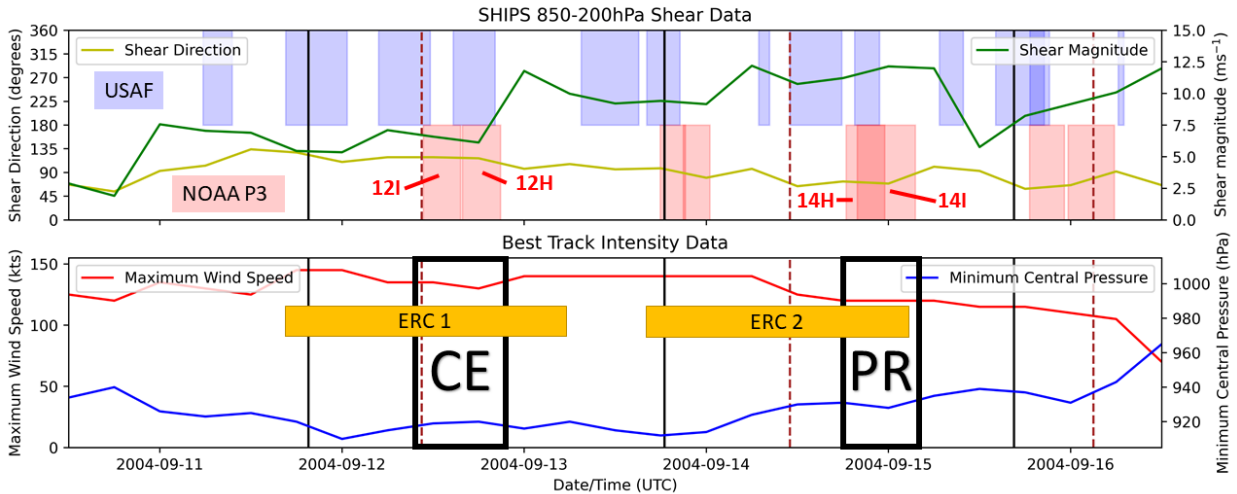
10

FIG. 2. (Top) 850-200 hPa environmental (0-500 km radius) wind shear direction and magnitude, obtained from SHIPS analysis spanning 1200 UTC 10 Sep to 1200 UTC 16 Sep. Shear direction is expressed as a vector heading (90° points to the east and increases counter-clockwise). Blue rectangles show times for USAF missions into the storm, and red rectangles for the P3 missions (labeled in red). Thin black lines denote SEF times and dashed burgundy lines are the Maximum Wind Transition (MWT) times (see text for details). (Bottom) Maximum wind speed and minimum central pressure from NHC Best Track Data. Orange boxes indicate time spans of the ERC1 and ERC2 events. Thick black boxes denote the two periods discussed in sections 4 and 5, labeled CE (Concentric Eyewall period) and PR (Post-Replacement Adjustment period), respectively.

at least an 8 m s^{-1} difference from the strongest eyewall in each mission. ERC2 lacks this clear azimuthal average wind minimum in the moat. Additionally, at the end of ERC2 the maximum average wind weakens about 5 m s^{-1}.

This study uses TDR data from the P3 missions on 12 Sep and 14 Sep (mission names shown in Table 1) which cover different stages of ERC1 and ERC2. P3 missions on 12 Sep cover the Concentric Eyewall period, and missions on 14 Sep and 15 Sep are used to study the Post-Replacement Adjustment period. The P3 missions at the end of 13 Sep (at the start of ERC2) occur too early in the ERC to be considered for study within the scope of this paper.
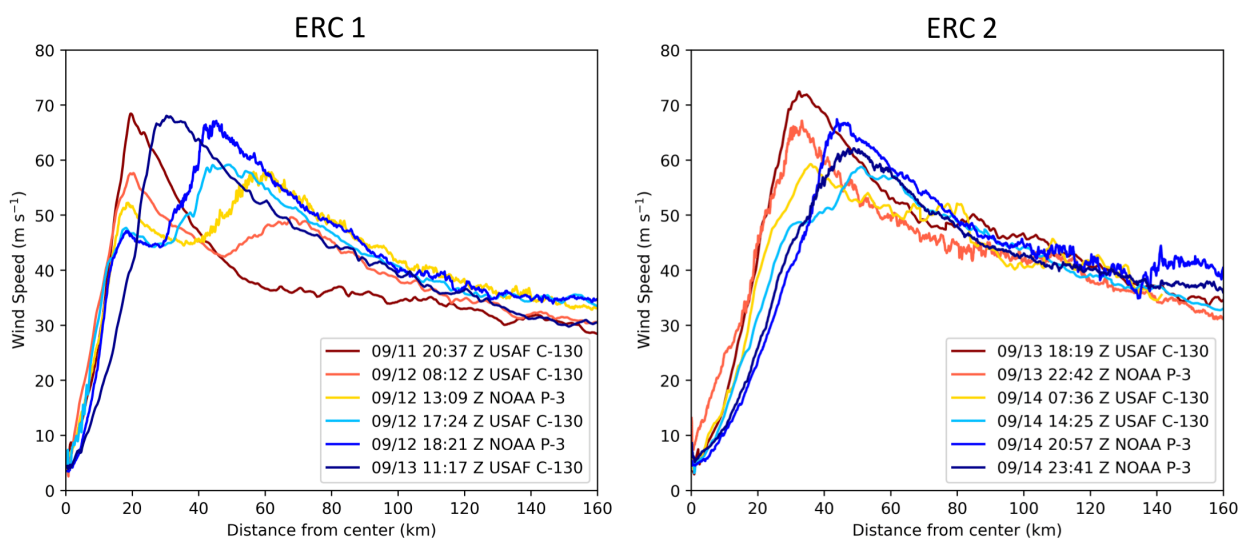
11

FIG. 3. Radial profiles of azimuthally averaged wind speeds from 700 hPa flight-level data from both USAF and P3 aircraft for ERC1 and ERC2. The legend shows the time halfway between the start and end time of the mission (start and end times of the P3 missions used in the study are included in Table 1).

12

4. Concentric Eyewall Period

The first P3 mission in the Concentric Eyewall period, 12I, occurs about 17.5 hours after ERC1's SEF (1935 UTC 11 Sep) and just after the outer eyewall tangential wind maximum surpassed that of the inner eyewall at 1030 UTC 12 Sep (period labeled "CE" in Fig. 2). Around this time (1309Z), the outer eyewall has the primary wind maximum seen in the flight level azimuthally averaged winds at around 58 km radius (Fig. 3a).
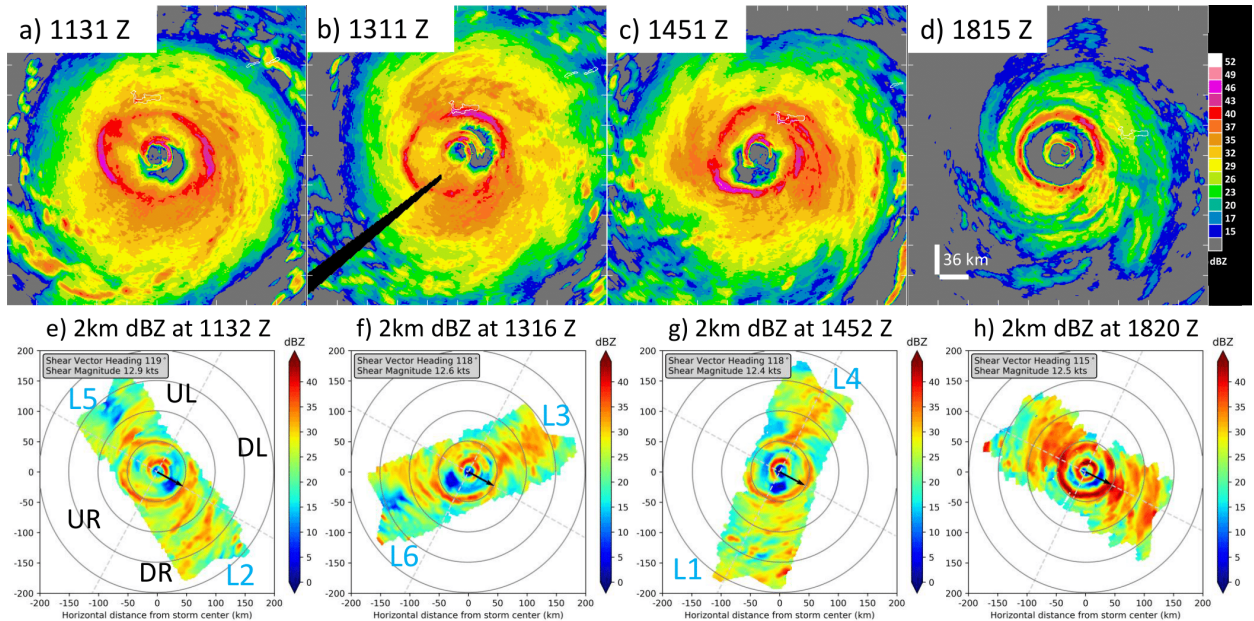

FIG. 4. (a-d) LF radar scans showing reflectivity around 2 km altitude for ERC1. Tick marks around panel borders show 36 km length spans. LF images are courtesy of HRD. (e-h) TDR 2-km reflectivity from individual swath analyses. Range rings in gray are every 50 km from the storm center. The shear vector is shown in black and shear-relative quadrants are indicated by the dashed lines and labeled in black. Radial leg label numbers are in blue followed by an "L" for the swaths in e-g. Data are from P3 aircraft missions 12I [(a-c),(e-g)] and 12H [(d),(h)] on 12 Sep.

Figure 4 shows radar reflectivity plan views from missions 12I and 12H. No calibration was performed for the reflectivity values between 12I and 12H, but this does not affect the current analysis since all reflectivity comparisons are made between azimuthal locations within a particular mission and not between missions. Each leg of mission 12I is labeled in blue starting in the DR quadrant and leg numbers increase cyclonically downwind. Figures 4a, b, e and f from 12I show that the outer eyewall has an elliptical shape, with a major axis diameter of 120 km and a minor

13

axis diameter of 95 km (approximated from LF imagery). An ellipse is a manifestation of a wavenumber-2 asymmetry. This wavenumber-2 reflectivity signal in the outer eyewall rotates cyclonically in animations of the LF data (not shown). Five hours later, the outer eyewall has shrunk in radius and has become more circular as seen in Fig. 4d and h from 12H.

The shear vector points to the ESE with a moderate magnitude of 6.5 m s^{-1} for the duration of 12I and 12H. Figures 4e and f show the TDR swaths at 1132 UTC and 1316 UTC where the left-of-shear side of the inner eyewall has much higher reflectivity values compared to the right-of-shear side. Figure 5 shows the convective-stratiform separation performed on the swaths of mission 12I. The convective-stratiform separation algorithm follows the methodology of Alvey et al. (2020). The analysis shows that moderate to deep convection is more present on the left-of-shear side for the inner eyewall. This asymmetry is also observed by the LF scans where the southern portion of the inner eyewall is weaker (Fig. 4a) or even open (Fig. 4c). This open eyewall along with increased reflectivity in the northern portion of the inner eyewall is a clear wavenumber-1 precipitation asymmetry. These wavenumber-1 asymmetries are consistent with previous work on shear-relative eyewall asymmetries (e.g., Reasor et al. 2000; Chen et al. 2006; Hence and Houze 2011; Didlake and Kumjian 2018). A sheared vortex will experience asymmetries of isentropic surfaces leading to rising and sinking motions right-of-shear and left-of-shear, respectively (Jones 1995; Frank and Ritchie 1999). These asymmetries can also be explained by differential vorticity advection processes in a sheared vortex, resulting in the strongest upward motions in the downshear half (Bender 1997; Frank and Ritchie 1999, 2001). These dynamics result in the precipitation maximum left-of-shear observed in Ivan's inner eyewall at this time, and is consistent with many past studies (Black et al. 2002; Chen et al. 2006; Eastin et al. 2005; Reasor et al. 2013; DeHart et al. 2014; Foerster and Bell 2017; Hence and Houze 2011; Homeyer et al. 2021; Boehm and Bell 2021). Radially outward from the inner eyewall, there is a persistent inner core rainband attached to the inner eyewall, seen in the NE sector of the moat in Figs. 4a, b and d.

The above processes of shear-induced asymmetric forcing rely on the vortex to tilt in response to the shear. Previous studies find that vortex tilt and vertical wind shear directions are strongly correlated, with the tilt generally being pointed downshear-left (Reasor et al. 2004; Reasor and Eastin 2012; Reasor et al. 2013; Fischer et al. 2022). But the tilt is not always cleanly pointed in that direction, especially during tilt precession (e.g. Stevenson et al. 2014). Vortex tilts were

14

obtained from the TC-RADAR database (detailed in Fischer et al. 2022) and showed small tilt magnitudes (3-5 km during 12I, and 7-13 km in 14I) with directions pointed in the DL quadrant (not shown), consistent with the results of Fischer et al. (2022) for major hurricanes. Given that the tilt direction remained in the expected shear-relative location (DL), it appears that there is no vortex tilt mechanism independent from the shear forcing that is altering the max updraft locations.
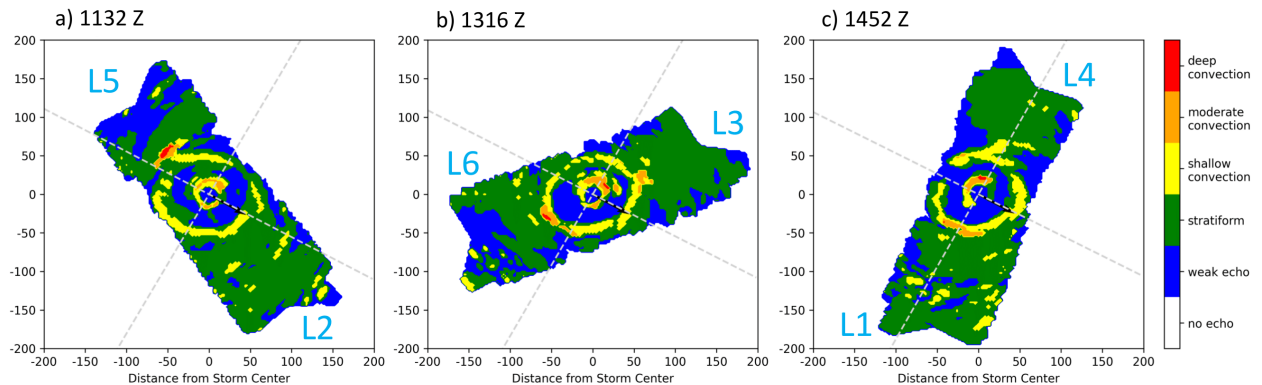

Fig. 5. Results of convective-stratiform separation for the three swaths in mission 12I. Radial leg label numbers are in blue.

Interestingly, despite being in a phase of weakening inner eyewall tangential winds, the opening in the inner eyewall temporarily becomes filled in around 1820 UTC (Figs. 4d and h). The other swath times during the 12H mission show a similar asymmetry to the one seen and described in 12I (not shown). The exact position and amplitude of the asymmetry varies slightly from swath to swath, but the inner eyewall reflectivity maximum remains in the left-of-shear half during both 12I and 12H.

It is difficult to confidently assess the presence of a wavenumber-1 asymmetry in the outer eyewall reflectivity in either the TDR or LF reflectivity fields because the inner eyewall wavenumber-1 asymmetry led to inconsistent attenuation of the radar beam around the storm. Figure 6 shows 85-89 GHz microwave imagery during the Concentric Eyewall period. In the outer eyewall, a region of warmer brightness temperatures is generally seen in the UR (southwest) quadrant. This signal corresponds to weaker deep convection in the UR, and indicates a wavenumber-1 asymmetry in the outer eyewall precipitation.

The more axisymmetric nature of the outer eyewall compared to the asymmetric inner eyewall is consistent with Hence and Houze (2012)'s composite study of concentric eyewalls. They found
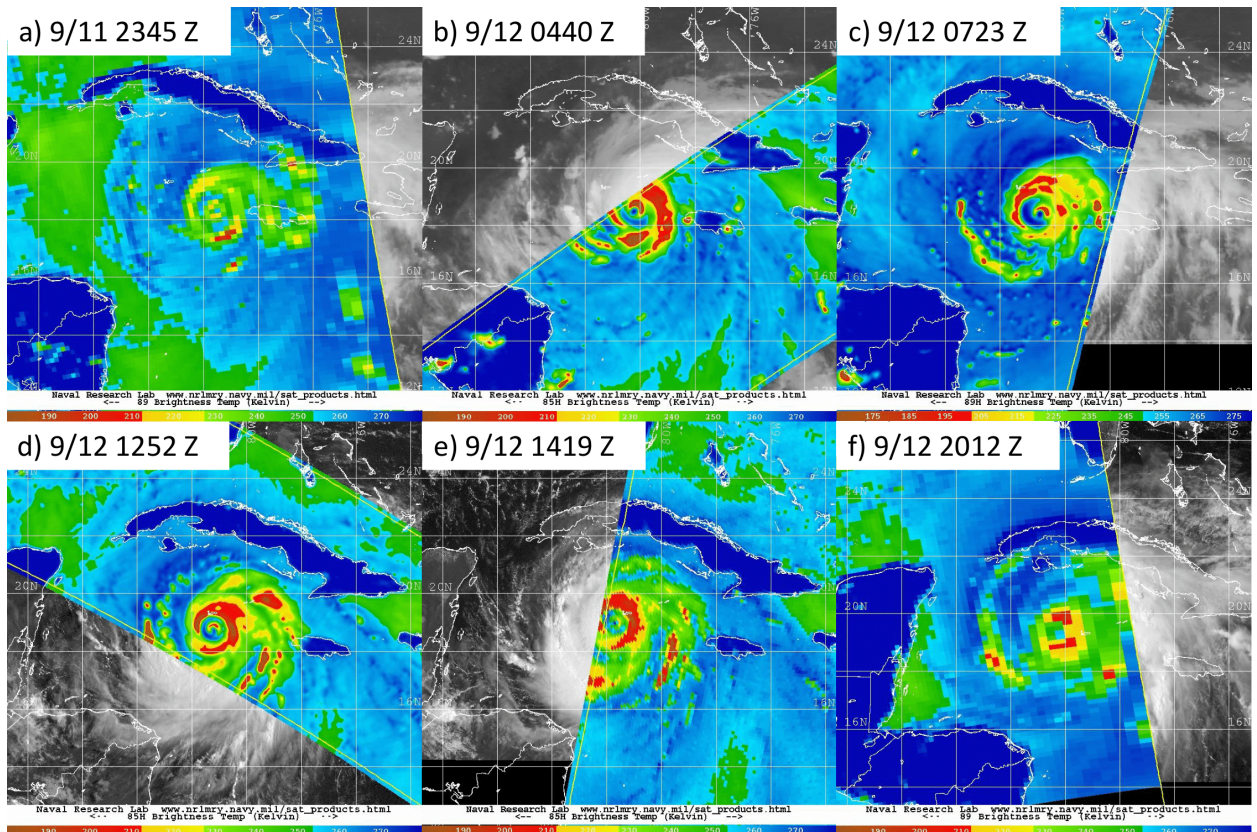
15

FIG. 6. 85-89 GHz microwave brightness temperature imagery of Hurricane Ivan at (a) 2345 UTC on 11 Sep, and (b) 0440 UTC, (c) 0723 UTC, (d) 1252 UTC, (e) 1419 UTC, (f) 2012 UTC on 12 Sep. Background geostationary images are from GOES-12 infrared (a-c) and visible (d-f). Microwave sensors are the AMSU-B (a and f), TMI (b and d), AMSRE (c), SSMIS (e). Images are from the Naval Research Laboratory Monterey Tropical Cyclones webpage (http://www.nrlmry.navy.mil/TC.html)

the outer eyewall was more resistant to shear asymmetries, with only a slight asymmetry favoring precipitation left-of-shear, while the inner eyewall showed a more substantial asymmetry.

In order to better understand the forcings for the outer eyewall reflectivity asymmetry, we seek to identify kinematic asymmetries that potentially contribute to the asymmetric precipitation field. Specifically, we choose to look for regions of mesoscale descending inflow (MDI) typically found just radially outward of rising outflow in stratiform TC rainbands. We define the MDI as a mesoscale feature of overlapping radial inflow and downward motion occurring on a horizontal spatial extent of >20 km (meso-β scale). Previous studies have established a crucial link between the MDI in the left-of-shear stratiform rainband and SEF (Didlake and Houze 2013; Qiu and Tan 2013;
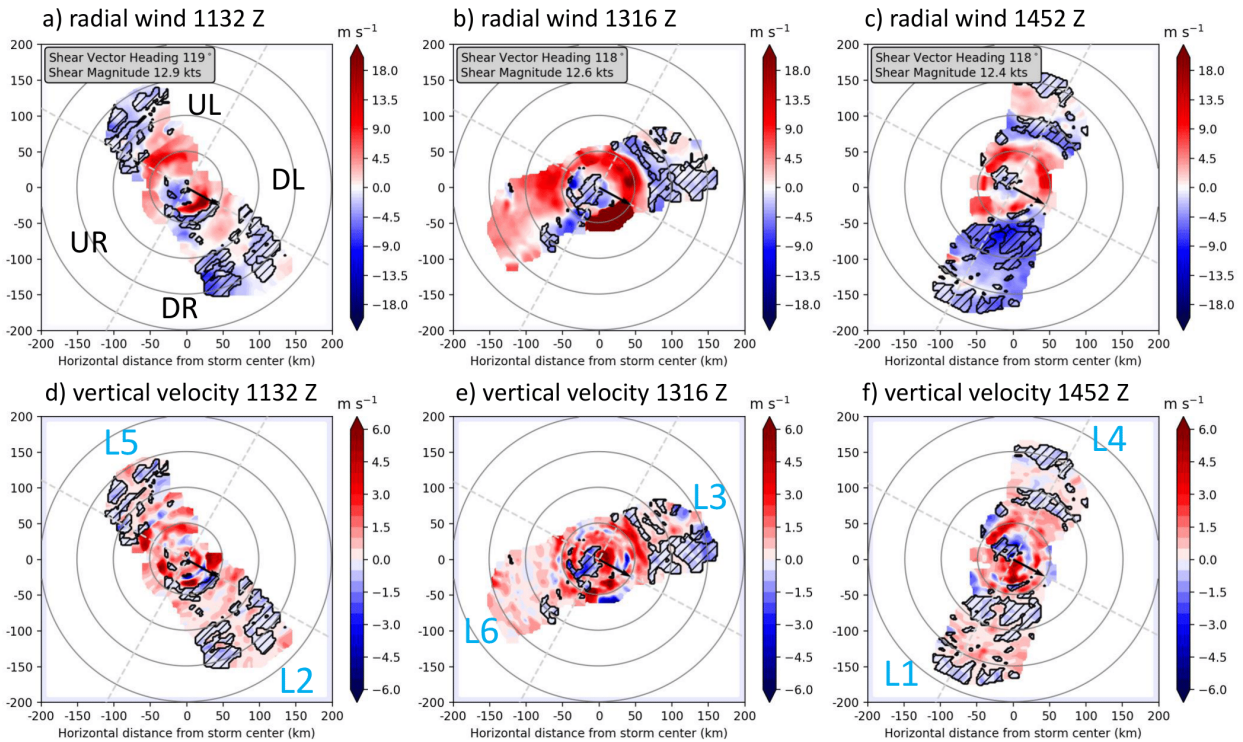
16

FIG. 7. Swath plan views at 3 km altitude of radial velocity (a-c) and vertical velocity (d-f) from mission 12I. Hatched black contours show regions where both radial velocity and vertical velocity are negative. Range rings in gray are every 50 km from the storm center.

Didlake et al. 2017, 2018; Yu et al. 2021, 2022; Wang and Tan 2022; Zhu et al. 2022). The MDI forms when melting and evaporative cooling within the stratiform rainband forces air to become negatively buoyant and draws in environmental air at the midlevels. This MDI then descends into the boundary layer, where it forces new updrafts via cold pool dynamics (Yu and Didlake 2019). These persistent convective updrafts left of shear help to generate sufficient convection that is advected around the upshear quadrants to help form the secondary eyewall. Modeling studies (Yu et al. 2021, 2022; Wang and Tan 2022; Zhu et al. 2022) suggest the possibility that these left-of-shear updrafts can also persist after SEF due to continued stratiform precipitation and MDI left of shear.

Figures 7 and 8 show plan views (3 km altitude) and swath averages of radial wind and vertical velocity during mission 12I. Also shown are hatched contours (black in Fig. 7 and gold in Fig. 8) that highlight regions of overlapping negative vertical velocity and negative radial velocity, which
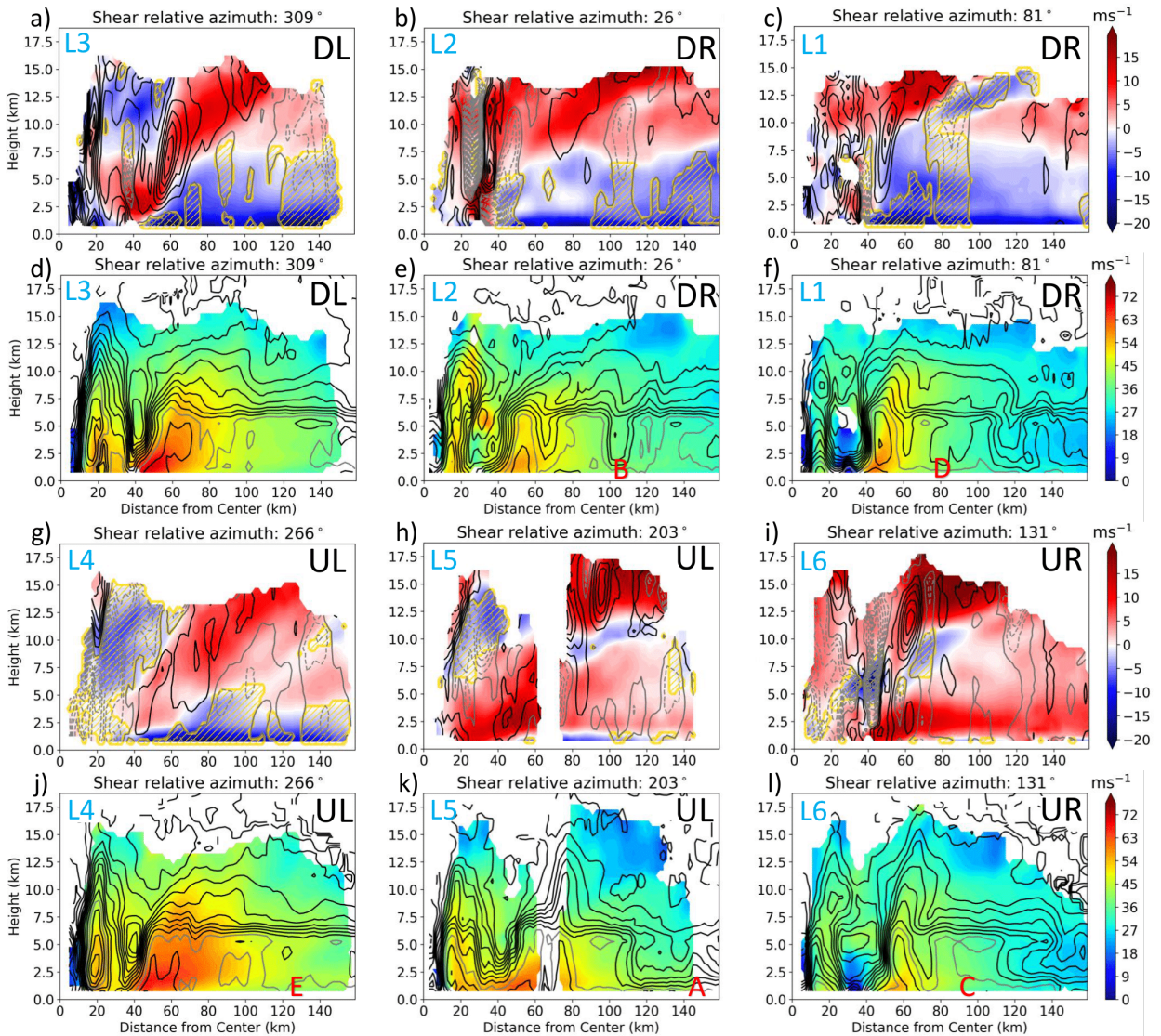
17

FIG. 8. Swath average cross sections of 30° sectors for each radial leg of mission 12I. (a-c, g-i) Radial velocity (shaded) with vertical velocity contoured (updrafts in solid black, every 1 m s^{-1}, downdrafts in dashed gray every 0.5 m s^{-1}, zero contour in solid gray). Hatched gold contours show regions of negative vertical and radial velocities. (d-f, j-l) Tangential velocity (shaded) with reflectivity contoured every 3 dBZ in black, with 30 dBZ contour in gray. All winds are storm relative. The locations of selected dropsondes are labeled with red letters.

are potentially MDI regions. Although all regions of descending inflow are highlighted, the regions of interest are particularly in the vicinity of the outer eyewall and the rainband regions of the storm, where forcings for descending inflow are likely a result of the MDI processes mentioned above. In this TDR analysis, a steady state is assumed in the TC during a single mission to allow for

comparison of the swaths at different times. The features of focus in this study are mesoscale in nature which we assume evolve at a slower rate than the time spans between each swath, and so should not differ much between swath times.

In the left-of-shear half, just radially outward from the outer eyewall, inflow is present in legs L3 and L4 between 70-110 km radius (Fig. 7b and c). In the swath average of leg L3 (Fig. 8a), the low- to mid-levels (2-7 km altitude) show strong inflow reaching 8 m s^{-1} that slopes downward and meets strong outflow reaching 6 m s^{-1} around 60 km radius (the outer eyewall radius), and appears to be feeding into the outer eyewall maximum updraft of 8 m s^{-1}. This deep inflow overlaps with downward motion at intermittent radii, where the strongest swath averaged downdraft is 0.5 m s^{-1} near 140 km radius. The 3 km plan view (Fig. 7e) shows that this descending inflow is actually a broad, nearly contiguous region stretching across all azimuths in the DL quadrant. The vertical velocities through the center of the swath along the flight track are often prone to error due to the sampling and retrieval technique (e.g., Didlake and Houze 2009). The positive vertical velocities reaching 2.5 m s^{-1} through the center of the swath are possibly erroneous, and they potentially obscure the spatial extent and magnitude of the descending inflow in the swath average. This descending inflow feature is mesoscale in nature, having a radial and/or azimuthal extent of >20 km. Given its characteristics and location within stratiform precipitation (Fig. 5b), this feature is likely similar to MDIs found in previous observational (Didlake and Houze 2013; Didlake et al. 2017, 2018; Fischer et al. 2020) and modeling studies (Qiu and Tan 2013; Yu and Didlake 2019; Yu et al. 2021, 2022; Wang and Tan 2022; Zhu et al. 2022).

An MDI region is also seen downwind in leg L4 with overlapping swath-averaged inflow and downward motion below 5 km altitude and between 80-100 km radius (Fig. 8g). L4 straddles both UL and DL quadrants, and the descending inflow region at 3 km altitude extends across most azimuths within the swath (Fig. 7f). We note again that L4 shares similarities in its swath-averaged secondary circulation pattern as L3, with a downward-sloping inflow pattern that meets rising outflow at the radius of the outer eyewall. That being said, in leg L4 the inflow and outflow are weaker (less than 5 m s^{-1} in magnitude), shallower (below 5.5 km altitude), along with a weaker updraft (0-2 m s^{-1}) (Fig. 8g) compared to L3 (Fig. 8a).

Downwind of leg L4, leg L5 has smaller patches of descending inflow at 3 km (Fig. 7d), which do not prominently appear outside of the outer eyewall in the swath average (Fig. 8h).

19

The UR quadrant shown in leg L6 (Fig. 8i) has higher-altitude descending inflow between 60-75 km radius feeding into the outer eyewall updraft from 6-11 km altitude, yet the low levels have a more mixed vertical motion field. Downwind in the DR legs, L2 and L1 (Figs. 8b,c), strong BL inflow (reaching 18 m s^{-1}) is present below 2 km altitude, and may be feeding into the updrafts cyclonically downwind. Leg L2 (Fig. 8b) shows descending inflow regions between 90-150 km radius, but these are not adjacent to an outer eyewall updraft as in other legs. Leg L1 (Fig. 8c) does have a mid- to low-level region of descending inflow between 50-70 km radius and an adjacent outer eyewall updraft between 40-50 km radius.

In the inner eyewall at 18 km radius, updrafts reaching 6 m s^{-1} extend from the lowest level to over 13 km altitude in the downshear quadrants (Figs. 8a-c). Notably the DL leg L3 (Fig. 8a,d) corresponds to the LF scan in Fig. 4b when the moat rainband is clearly present and a reflectivity tower (maximum of 30 dBZ) is present between 25-35 km radius in the moat region. Updraft contours bulge upwards and radially inwards below 6 km altitude between 25-35 km radius (Fig. 8a), corresponding to the location of the moat rainband at 1311 UTC (Fig. 4b). The inner eyewall in the upshear quadrants is largely comprised of deep downdrafts, reaching values < -2 m s^{-1} between 15-25 km radius (Figs. 8g-i). This inner eyewall vertical velocity asymmetry supports the precipitation asymmetry mentioned earlier, where precipitation grows in the downshear updraft and is azimuthally advected downwind to the left-of-shear quadrants to produce the local reflectivity maximum (Figs. 4 and 8d,j,k between 15-25 km radius). The upwind position of the updrafts and downwind position of the downdrafts relative to the reflectivity maximum has also been observed in the inner eyewall during the ERCs of Hurricane Gilbert (1988) (Black and Willoughby 1992; Dodge et al. 1999) and Hurricane Alicia (1983) (Marks and Houze 1987).

Figure 9 displays the mission-averaged 2.5-4 km radial velocity and vertical velocity by shear-relative azimuth, along with the descending inflow contours in gold. Many of these descending inflow regions are >20 km in horizontal extent, and thus are identified as MDI regions. Parts of these MDI regions match those seen in Figs. 7 and 8. We highlight four broad areas or individual regions of MDI in this discussion. First, starting in the DR quadrant between 45-100° shear-relative azimuth, two MDI regions span from beyond 90 km radius to meet the outer eyewall at 57 km radius (Fig. 9). These features correspond to the descending inflow in L1 in the same radial range (60-90 km) in the swath-mean cross-sections (Fig. 8c) and plan view (Figs. 7c,f). Second, downwind

20

between 0-50° shear-relative azimuth, Fig. 9 shows MDI regions occurring at larger radii (90-160 km) that are not connected to the outer eyewall. These MDI regions can also be seen in Figs. 7a, d, and 8b in the DR quadrant of leg L2 at the same radii. Third, further downwind between 300°-330°, Fig. 9 shows MDI regions that extend from far radii (~150 km) and nearly reach the outer eyewall. These regions correspond to the descending inflow regions of leg L3 shown in Figs. 7b, e, and 8a, with downdrafts embedded in the deep inflow between 60-110 km radius. Fourth, Fig. 9 shows another MDI region centered around 270° between 70-110 km radius. This region corresponds to leg L4's descending inflow in the same radial range in Figs. 7c, f, and 8g.

Each of these four MDI areas have their radially inner ends near regions of enhanced low-level convergence that can be seen in Fig. 9. The second MDI area (0-50°) terminates at a region of low-level convergence $> 2 \times 10^{-4}$ s^{-1} at 85 km radius and 35° shear-relative azimuth (Fig. 9). This low-level convergence is collocated with enhanced updrafts of around 0.5 m s^{-1}. These features are associated with a rainband connected to the outer eyewall that can be seen in Fig. 4e in the DR quadrant of leg L2. Correspondingly, both the enhanced low-level convergence and updrafts in Fig. 9 can be traced inwards to where it meets the outer eyewall at a convergence maximum around 315° and updraft maximum of ~ 2.5 m s^{-1} (Fig. 9b). The third MDI area (300°-330°) also connects to this same outer eyewall convergence and updraft maximum.

Downwind, the fourth MDI area (270°) is connected to continued convergence and updrafts (>1 m s^{-1}) at the outer eyewall. In the outer eyewall region between 45-65 km radius, the left-of-shear half sees stronger updrafts as a result of this enhanced convergence. Comparatively, the right-of-shear quadrants have weaker average updraft magnitudes: the mean values in the 2.5-4 km altitude layer from 45-65 km radius are 1.8 and 1.11 m s^{-1} in the DL and UL, compared to 1.04 and 0.44 m s^{-1} in the UR and DR, respectively.

Overall, this inward spiraling convergence feature and associated enhanced updraft appear to be the result of multiple MDI regions starting in the DR quadrant (45°) (Fig. 8b) and extending into the DL and UL at 60-100 km radius (Fig 8a, g). This broad pattern of MDI regions occurs within stratiform rainband precipitation (Fig. 5) outside the outer eyewall. These observed features are consistent with previous observations of a left-of-shear MDI that is driven by stratiform-rainband cooling and leads to locally enhanced updrafts via cold pool dynamics. But in our case, the stratiform MDI regions are remnant features after SEF possibly with similar dynamics, and result

in locally enhanced updrafts in the outer eyewall. Their observed close proximity suggests that these dynamical connections seen in modeling studies are also present here in Ivan.

Available dropsondes were analyzed in an attempt to identify downdrafts and cold pools associated with MDI regions. Figure 10 shows the five dropsondes released during mission 12I in the inner core region radially outside the outer eyewall (60-150 km radial range). Their locations are denoted with red letters in Fig. 8 and in white letters in Fig. 9. Unfortunately, no dropsondes were released in this radial range of the DL leg (L3). Dropsondes available in the rainband region from other quadrants were chosen to try to identify other rainband-induced cold pools or any larger-scale thermodynamic asymmetries present during the mission. Downdrafts can be identified in the soundings where there is a sharp separation of the temperature and dew point temperature lines along with more adjacent temperature lines above and below; this is a so-called "onion sounding" signature (Zipser 1977). Miniature versions of these signatures are visible in dropsondes B and E (legs L2 and L4) between 850-935 hPa and 840-880 hPa, respectively (Fig. 10b, e). Dropsonde B has a more prominent onion signature, with a dew point temperature increase of ~2 °C near 925 hPa and a corresponding potential temperature decrease of 2 °C. This profile is squarely within an MDI (with -12 m s^{-1} radial velocity and -0.25 m s^{-1} vertical velocity) in the DR (Fig. 8b). Without temperature profiles of the immediate surroundings, it is not clear if this descending air is indeed part of a cold pool. Dropsonde E occurs in between downdrafts with zero vertical motion (Fig. 8g), which probably explains the subtle downdraft signature in the profile.

We next search for a vortex-scale low-level temperature asymmetry by plotting all five dropsonde temperatures together in Fig. 10f. The uppermost extent of the onion signature in dropsonde E is near 825 hPa. Below 825 hPa, the UL quadrant profiles (A and E) are generally cooler than the right-of-shear dropsondes (B, C, D), where the largest temperature difference (2 °C) occurs at 915 hPa between A and C. In a composite TC dropsonde study, Nguyen et al. (2019) showed that in weak TCs (≤ category 1 strength), below 1 km altitude, the right-of-shear quadrants have warmer potential temperatures than the left-of-shear quadrants, with a maximum difference of 1.2 °C. Zhang et al. (2013) found the same temperature asymmetry at 50 m height in the eyewall region of hurricane strength storms, with a maximum temperature difference of 0.4°C. The current dropsondes are consistent with this temperature asymmetry, notwithstanding a contradicting DL profile. Several studies attribute a corresponding equivalent potential temperature asymmetry to

convective downdrafts (e.g., Riemer et al. 2010, 2013); it is unclear here in Ivan if MDI regions can account for the observed temperature differences.

Overall, the Concentric Eyewall period showed an inner eyewall asymmetry with downshear updrafts and upshear downdrafts, resulting in a precipitation maximum left-of-shear. The outer eyewall asymmetry was more subtle, but still apparent. A series of MDI regions were found radially outward of an inward spiraling convergence zone in the downshear quadrants that produced a collocated updraft. This resulted in a stronger secondary circulation left-of-shear, which was strongest in the DL.
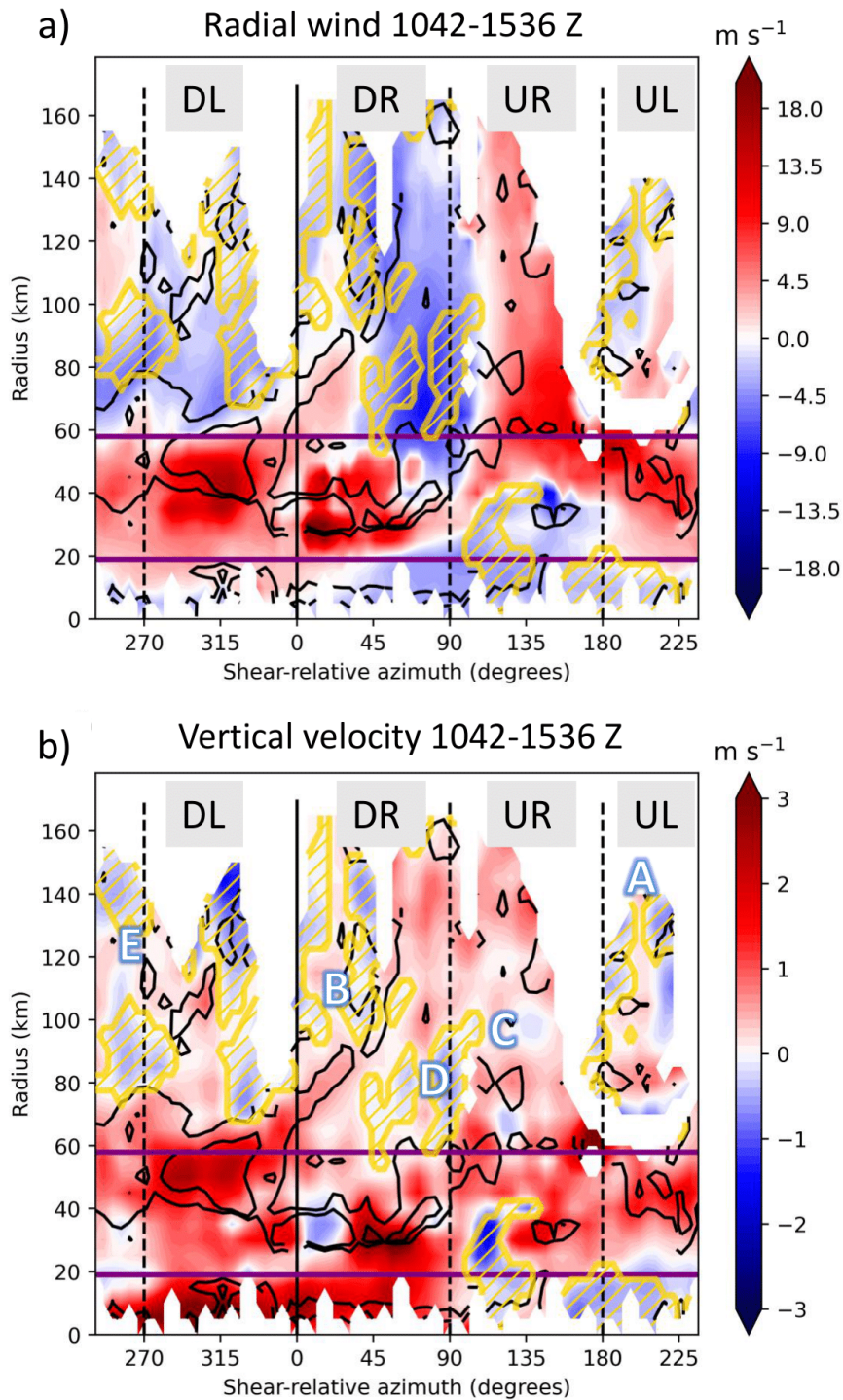
FIG. 9. Layer averages (2.5-4km altitude) of (a) radial wind and (b) vertical velocity (shaded) across radius and azimuth. Black contours show total convergence (0.5-3km average) contoured at 2×10^{-4} s^{-1} and 6×10^{-4} s^{-1}. Gold hatched contours are descending inflow regions. Shear-relative quadrants are separated by vertical lines. Horizontal purple lines are the inner and outer eyewall radii based on flight-level wind azimuthal averages. The left edge of the plot corresponds to the north direction, which is 241° shear-relative azimuth. Letters on panel b) show dropsonde locations for Fig. 10.

24
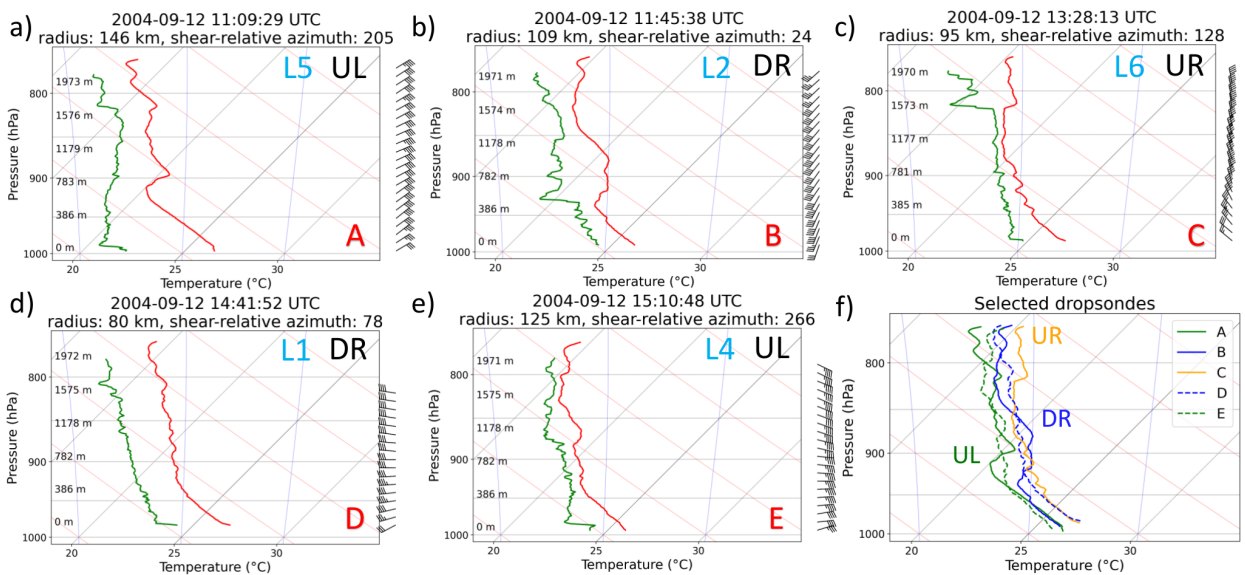
FIG. 10. (a-e) Selected inner core dropsonde profiles in mission 12I corresponding to the locations marked in Figs. 8 and 9b. Temperature is in red and dew point temperature in green. f) All five dropsonde temperatures plotted and colored by quadrant.

25

5. Post-Replacement Adjustment

Next, we focus on the inner-core asymmetries during the Post-Replacement Adjustment stage of a different ERC in Hurricane Ivan (Fig. 2). Around 2100 UTC 14 Sep, Ivan was nearing completion of ERC2. This stage was after the outer eyewall wind speed surpassed that of the inner eyewall, and the inner eyewall convection had begun to notably decay. The P3 mission 14I sampled the storm from 1945 UTC 14 Sep to 0330 UTC 15 Sep (box labeled "PR" in Fig. 2). One particular advantage of this period is the long duration of flight 14I, comprised of 6 swaths through the storm center. This flight spans the duration of the Post-Replacement period and allows us to use the same radar to compare radar reflectivity values without concern for differences in radar calibration between the two P3 aircraft. Focusing solely on data from 14I, we will compare data from the "Early" times (2043 UTC and 2159 UTC 14 Sep) to "Late" times (0203 UTC and 0307 UTC 15 Sep) during the mission to examine the evolution of the asymmetries of the new eyewall. Here we will address changes in the precipitation and vertical velocity maxima locations at the end of a replacement cycle.

a. Plan Views

Figure 11 shows the 2-km altitude reflectivity from the Early times (Figs. 11a, b) and the Late times (Figs. 11c, d) of mission 14I. At the Early times (Figs. 11 a, b) the outer eyewall is nearly an axisymmetric ring with a small opening at each time in different shear-relative locations. The remnants of the decaying inner eyewall convection can also be seen within 25 km radius, having a patchy, cellular appearance. At the Late times (Figs. 11c, d), the outer eyewall develops a more pronounced and consistent precipitation asymmetry. Here, the outer eyewall is much more open in the right-of-shear half, and reflectivity values are highest in the downshear direction at 0203 UTC and the left-of-shear direction at 0307 UTC. Also, the inner eyewall continues to decay, leaving only a small weak cell between 15-20 dBZ on the left-of-shear side.

Figure 12 shows the microwave imagery evolution surrounding the mission 14I. The inner eyewall can be last seen at 1302 UTC (Fig. 12a) on the eastern side, but by 1528 UTC (Fig. 12b) the inner eyewall brightness temperatures are not distinguishable from the brightness temperatures of the outer eyewall. The disappearance of the inner eyewall microwave signature occurs much earlier than in the TDR analyses (fig. 11). Additionally, the coolest brightness temperatures of the outer
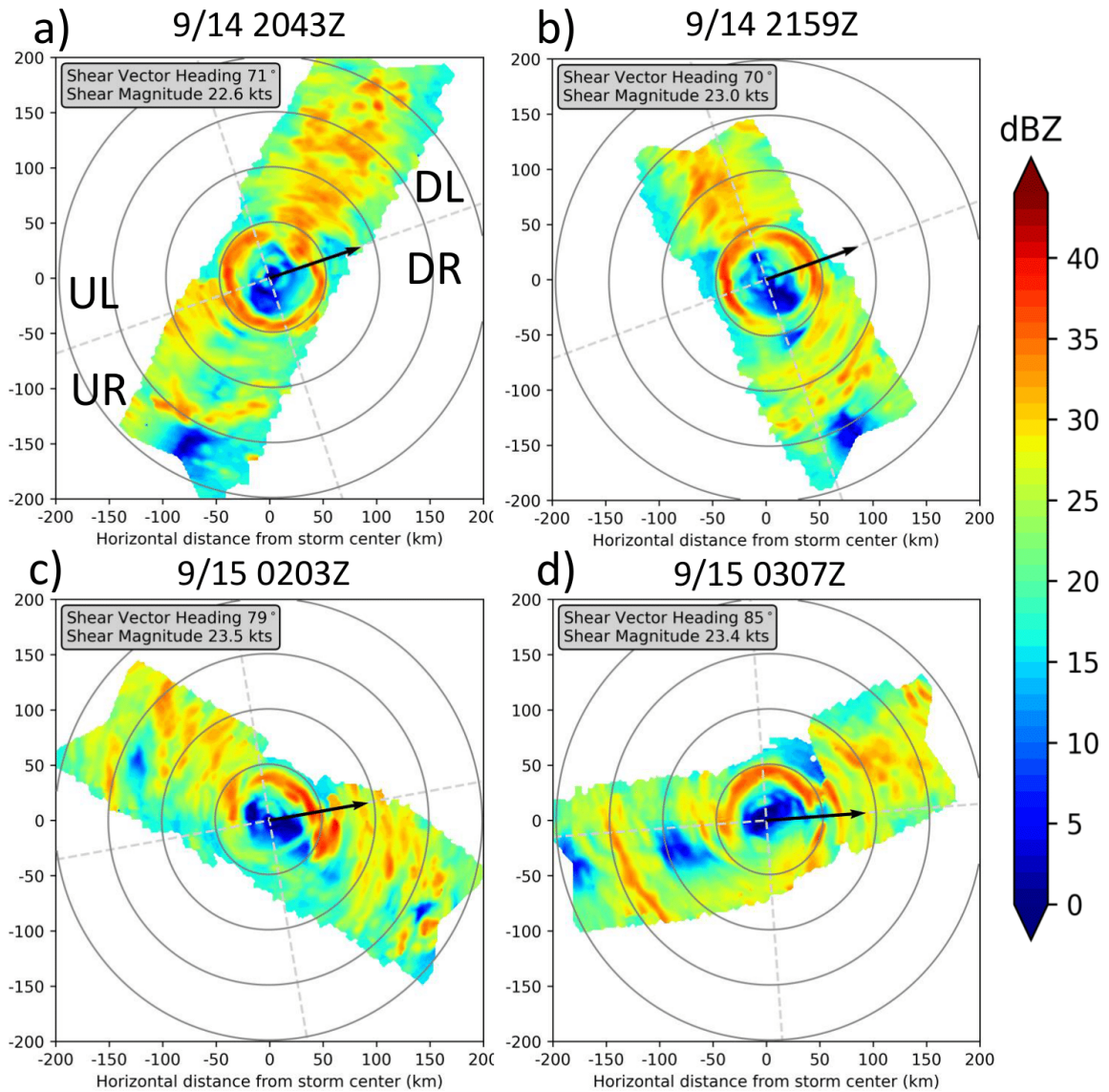
FIG. 11. 2-km plan view reflectivity from individual TDR swaths of mission 14I. Range rings in gray are every 50 km from the storm center. The shear vector is shown in black and shear-relative quadrant boundaries are dashed gray lines. Swaths belonging to the Early and Late swaths correspond to a, b and c, d, respectively.

eyewall begin on the northern side in Fig. 12a-c, but are seen on the eastern side at later times (Fig. 12d-f). This will be investigated further using the TDR analyses.
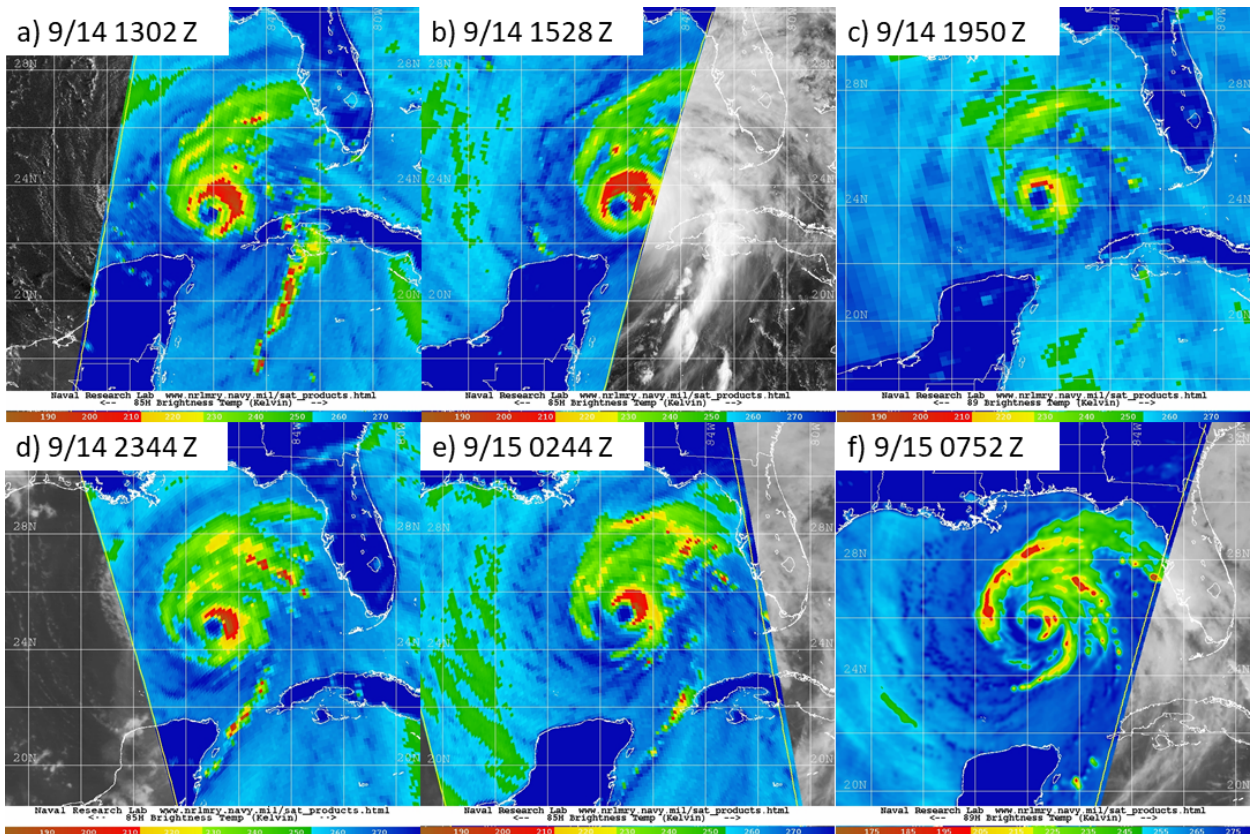
F_{IG}. 12. 85-89 GHz microwave brightness temperature imagery of Hurricane Ivan at (a) 1302 UTC (b) 1528
UTC, (c) 1950 UTC, (d) 2344 UTC on 14 Sep and (e) 0244 UTC (f) 0752 UTC on 15 Sep. Background
geostationary images are from GOES-12 Visible (a-c) and IR (d-f), and microwave sensors are the SSMIS 85
GHz (a-b, d-e), AMSU-B 89 GHz (c), and AMSRE 89 GHz (f). Images are from the Naval Research Laboratory
Monterey Tropical Cyclones webpage (http://www.nrlmry.navy.mil/TC.html)

b. Outer Eyewall CFADs

A more complete picture of the evolving eyewall asymmetry, both with the precipitation and
vertical velocity fields, can be attained by plotting the TDR data using contoured frequency by
altitude diagrams (CFADs; Yuter and Houze 1995). CFADs show the frequency distribution of
reflectivity and vertical velocity values at each vertical level. We will focus on the outer eyewall
during this Post-Replacement period. First, an annulus spanning from 25 km to 55 km radius
was chosen to capture the outer eyewall. Due to the inherent outward-sloping nature of hurricane
eyewalls (Stern and Nolan 2009; Rogers et al. 2012; Hazelton and Hart 2013; Hazelton et al. 2015)
and the fixed radii of the annulus, the upper portions (>10 km altitude) of the eyewall are observed

(not shown) not to be fully captured by our selected annulus. Additionally, data coverage and quality in the upper levels often suffers due to limited sensitivity below 10 dBZ and weak radar echoes from ice particles. This does not significantly affect the results as the focus will be below 10 km altitude.

Figure 13 presents CFADs of reflectivity and vertical velocity for the Early (Fig. 11a,b) and Late (Fig. 11c,d) periods of 14I. The reflectivity CFADs of the two times are quite similar with the most frequent reflectivities occurring between 12-18 dBZ and 8-11 km altitude (Fig. 13 a, b). The most notable difference is that the Late CFAD has an increase in frequency of 15-20 dBZ occurrences between 2-5 km altitude, meaning weaker reflectivities became more frequent in the Late times. The vertical velocity CFADs show that updrafts are much more frequent than downdrafts in the outer eyewall (Fig. 13 c, d). The velocity CFAD for the Early swaths has more 2-4 m s^{-1} updrafts in the midlevels between 3-10 km altitude when compared to the velocity CFAD for the Late swaths, decreasing the normalized frequencies from between 0.4-0.6 to between 0.25-0.4. Additionally, the Late period has more intense downdrafts (< -2 m s^{-1}) than the Early times, increasing the normalized frequencies from below 0.05 to between 0.1-0.15. Overall, the stronger updrafts in the Early period are in agreement with the corresponding stronger reflectivities.

c. Reflectivity CFAD Anomalies

Reflectivity CFAD anomalies were computed for each quadrant by first plotting each quadrant CFAD (not shown). Bin counts were similar across the different quadrants, allowing us to avoid data coverage biases in the quadrant CFADs. The total eyewall CFAD normalized frequencies (Fig. 13) were then subtracted from the normalized quadrant CFADs for the Early and Late periods to create the quadrant CFAD anomalies (Fig. 14). Positive anomalies indicate that the quadrant has a greater contribution of reflectivity occurrences to the total CFAD at that time, and negative anomalies indicate a smaller contribution to the total CFAD. For the Early times, the UL quadrant has a greater contribution to the total CFAD below 5 km altitude for stronger reflectivities (> 33 dBZ). For the Late times, the UL quadrant has a smaller frequency contribution for the same reflectivity values. Upwind, the DL quadrant exhibits a change from a positive anomaly for 25-35 dBZ and a negative anomaly for 35-40 dBZ below 7 km altitude in the Early times to a stronger overall positive anomaly above 25 dBZ at the Late times. Altogether, these differences represent an
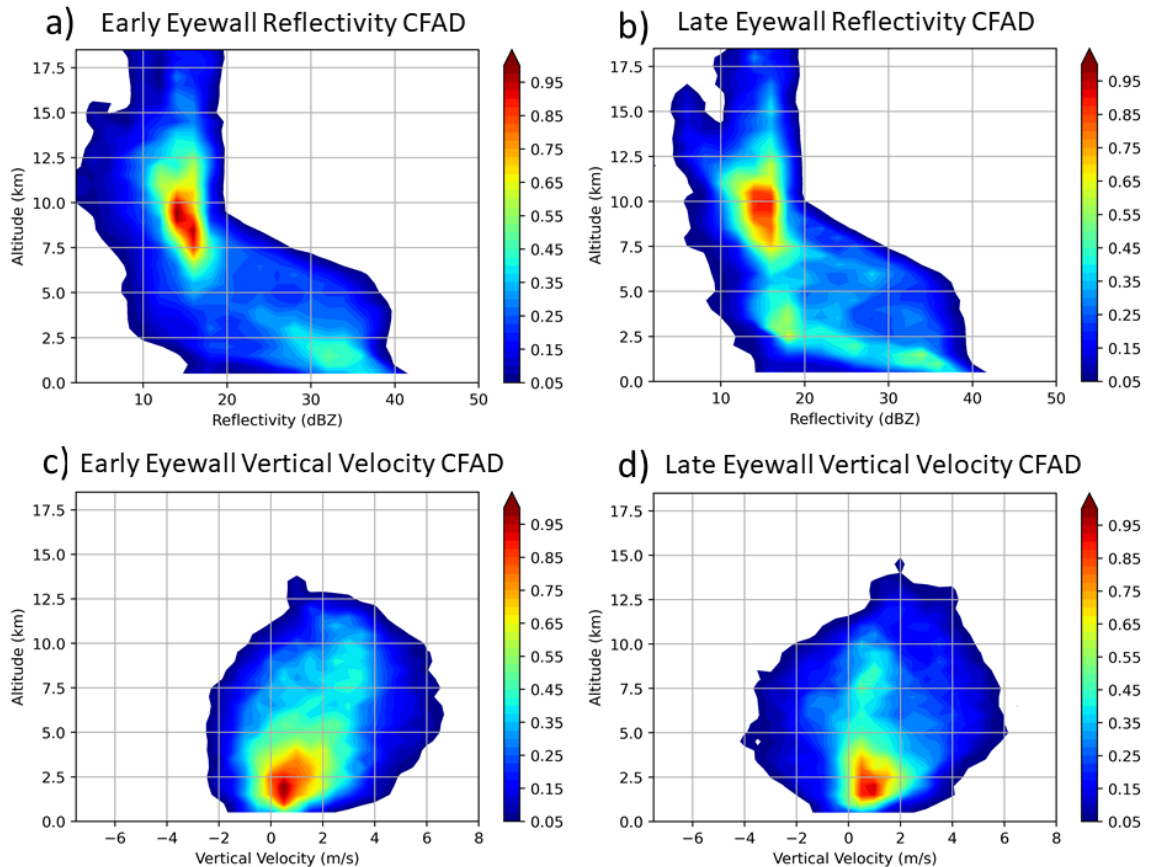
29

FIG. 13. (a-b) Contoured frequency by altitude diagrams (CFADs) of reflectivity for the outer eyewall (25-55 km radial range) during Early swaths (2043 UTC and 2159 UTC 14 Sep) and Late swaths (0203 UTC and 0307 UTC 15 Sep). (c-d) Vertical velocity CFADs shown for the Early and Late swaths. Frequencies are normalized by the CFAD maximum absolute frequency and so frequency values are unitless. Reflectivity CFADs were binned every 2 dB and velocity CFADs were binned every 0.5 m s^{-1}.

upwind shift in the highest outer eyewall reflectivities from the UL quadrant to DL quadrant. This finding, along with the stronger anomalies in the Late times, compares well with the plan views given the more asymmetric eyewall of the Late period residing predominantly in the DL quadrant (Figs. 11c and d). The DR quadrant has a consistent positive anomaly of high-end reflectivities at 5-10 km altitude. The UR quadrant is also largely similar at both times, with the only change being an increased contribution of weak reflectivities in the low levels.

30

d. Velocity CFAD Anomalies

The upwind shift in high reflectivity values, although subtle, is corroborated by the vertical velocity CFAD anomalies in Figure 15. The Early time DL quadrant (Fig. 15a) shows positive anomalies of the strongest updrafts at all altitudes. At the Late time, the DL quadrant anomalies show that the positive anomalies have shifted mainly to updrafts of 1-4 m s^{-1} below 8 km altitude. The strong, deep updrafts here have weakened and become less deep. On the other hand, the DR quadrant begins with positive updraft anomalies in the mid-levels, but over time, the DR quadrant develops a large increase in positive anomalies for strong updrafts, particularly in the mid- and upper levels in the Late swaths. This change in the position of the strongest eyewall updrafts suggests an upwind shift in the vertical velocity asymmetry. This shift in the downshear quadrants helps explain the shift in precipitation asymmetry discussed previously. In the Early time, precipitation formed in the stronger eyewall updrafts DL gets advected downwind by the strong tangential winds to form the UL high reflectivity positive anomaly. By the Late time when the stronger updraft is in the DR quadrant, the positive reflectivity anomaly follows and shifts upwind to the DL quadrant.

The upwind shift of the outer eyewall reflectivity and vertical velocity maxima is similar to the Post-Replacement upwind shift seen in the ERCs of Hurricane Gonzalo (Didlake et al. 2017). Gonzalo had a shift in the reflectivity and updraft maximum locations from left-of-shear to the downshear direction.

It is hypothesized that for the Early times, asymmetric rainband processes contribute to the outer eyewall vertical velocity asymmetry in the same manner as that proposed in Section 4 on the concentric eyewall asymmetries. That is, a spiral rainband complex with stratiform precipitation predominantly in the left-of-shear storm half forms an MDI and cold pool that helps to force persistent updrafts left-of-shear at its downwind end (Didlake and Houze 2013; Qiu and Tan 2013; Didlake et al. 2017, 2018; Yu et al. 2021, 2022; Wang and Tan 2022; Zhu et al. 2022). In this case, the downwind end of the rainband complex merges with the evolving outer eyewall and causes the DL frequency maximum in strong updrafts. But as the outer eyewall assumes the role of the singular eyewall in the storm, it interacts directly with the environmental wind shear and develops the wavenumber-1 asymmetry expected of single eyewalls. That is, vortex tilt processes and differential vorticity advection caused by the environmental wind shear lead to enhanced updrafts in the downshear quadrants (Bender 1997; Frank and Ritchie 1999, 2001; Braun et al. 2006; Reasor

31

et al. 2013). These effects apparently outweigh any impact of the rainband complex on the primary eyewall at this Late stage.

Overall, the upwind shift in the updraft maximum frequency going from DL to DR (and the corresponding reflectivity maximum just downwind) are likely a result of the eyewall asymmetry's dominating influence transitioning from rainband-driven effects to direct shear effects as the outer eyewall becomes the singular eyewall of the storm.
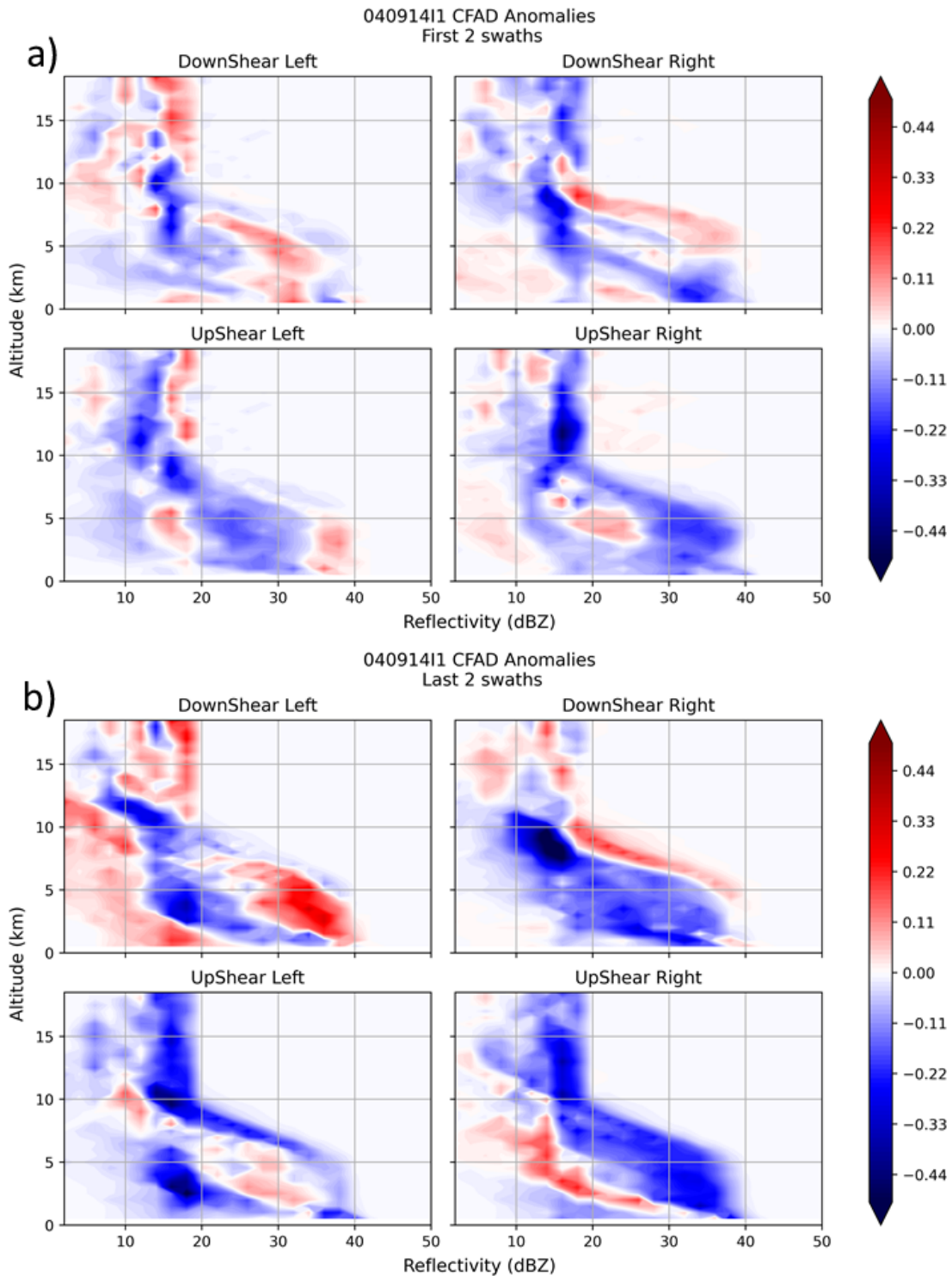
Fig. 14. Reflectivity CFAD anomalies of the outer eyewall by quadrant for the Early swaths (a) and the Late swaths (b). Values are unitless anomalies of normalized frequencies. Positive (negative) values indicate greater (fewer) occurrences relative to the total CFADs in Fig. 13a, b.
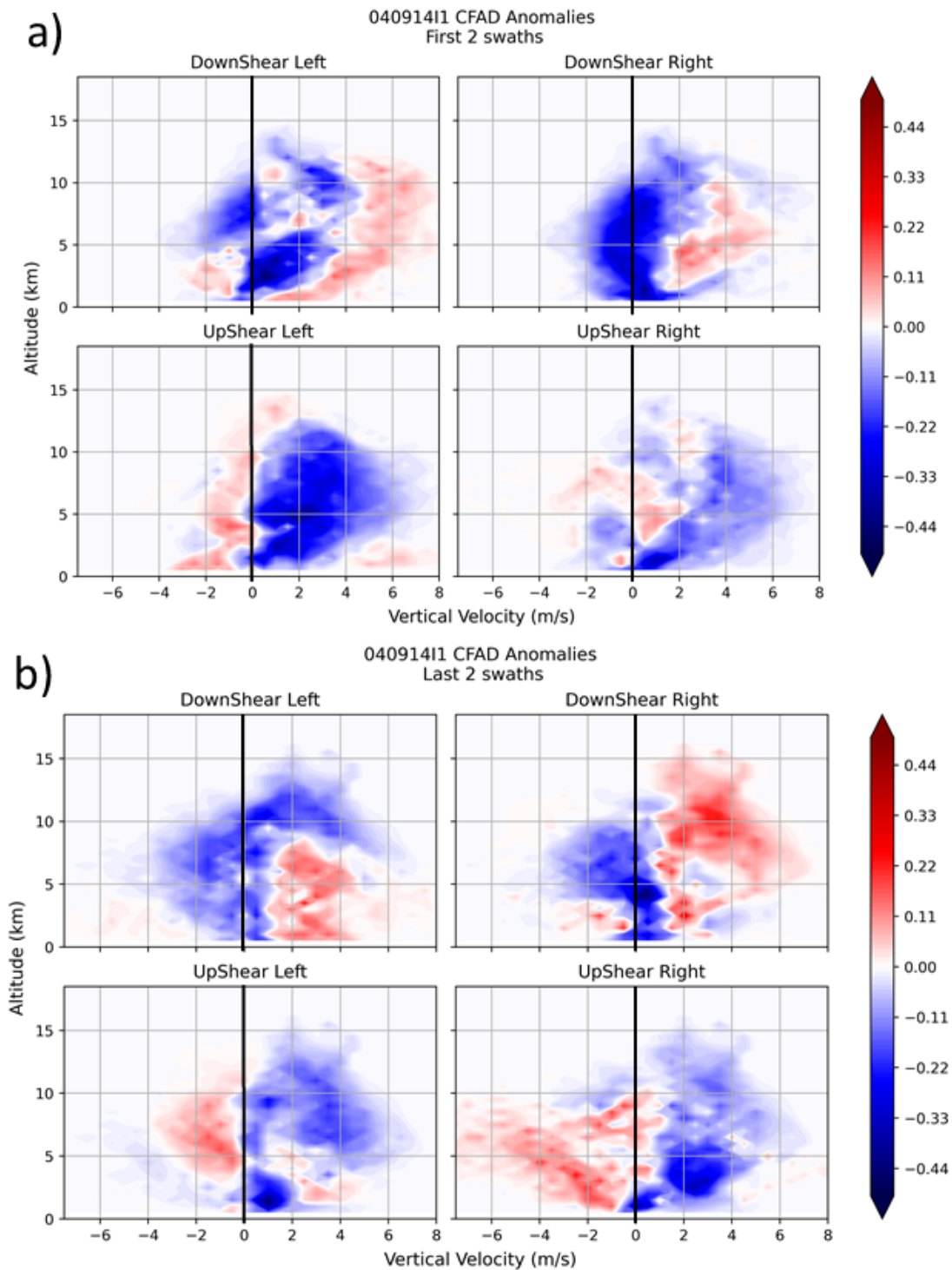
33

FIG. 15. As in Fig. 14, but for vertical velocity CFAD anomalies.

6. Discussion and Conclusions

Observations from reconnaissance aircraft (NOAA P3 and USAF C-130) and satellite microwave imagery were taken of the inner core of Hurricane Ivan (2004) as it underwent multiple successive eyewall replacement cycles (ERCs). The suite of airborne observations include Tail Doppler radar, lower-fuselage radar, 700 hPa flight-level observations, and dropsondes. This study analyzed the storm's kinematic and reflectivity structures during different stages of the ERCs to help improve our understanding of the structural changes that TCs experience during ERCs. Although the axisymmetric structure of a TC largely determines the storm's overall evolution, previous studies have suggested that asymmetric structures in the storm's eyewalls can provide important dynamical information about the onset (Judt and Chen 2010; Zhang et al. 2017; Wunsch and Didlake 2018; Didlake et al. 2018; Wang et al. 2019; Yu et al. 2021, 2022; Wang and Tan 2022), mature (Rozoff et al. 2008; Sitkowski et al. 2011; Hence and Houze 2012; Cheung et al. 2023), and end (Sitkowski et al. 2012; Didlake et al. 2017) stages of an ERC. Since storm asymmetries are often induced by and organized by the deep-layer (850-200 hPa) environmental wind shear, we analyzed the eyewall structures in storm quadrants defined by the wind shear vector. In this study, we focused on the mature (Concentric Eyewall) and end (Post-Replacement Adjustment) stages of two ERCs. The asymmetries within the inner and outer eyewalls at these stages are summarized in the conceptual model of Figure 16, and a hypothesis of the dynamical mechanisms that connect these observations is presented below.

Figure 16a illustrates the concentric eyewall structure during the mature ERC phase. The configuration of the reflectivity and vertical velocity asymmetries matches the findings from Didlake et al. (2017), where the strongest updrafts of the inner eyewall are upwind from the strongest updrafts of the outer eyewall. The updrafts of the inner eyewall are located downshear while the downdrafts are upshear, matching the same shear-relative asymmetry in a single eyewall experiencing environmental wind shear. Previous studies indicate that this vertical velocity asymmetry is due to direct interaction with the environmental shear, from differential vorticity advection (Bender 1997; Frank and Ritchie 1999; Reasor and Eastin 2012) and isentropic deformation processes (Jones 1995; Frank and Ritchie 1999, 2001; Braun et al. 2006; Boehm and Bell 2021). Meanwhile, the outer eyewall has updraft and reflectivity maxima in the left-of-shear quadrants. These maxima also coincide with mesoscale descending inflow (MDI) that stretches from stratiform precipitation at
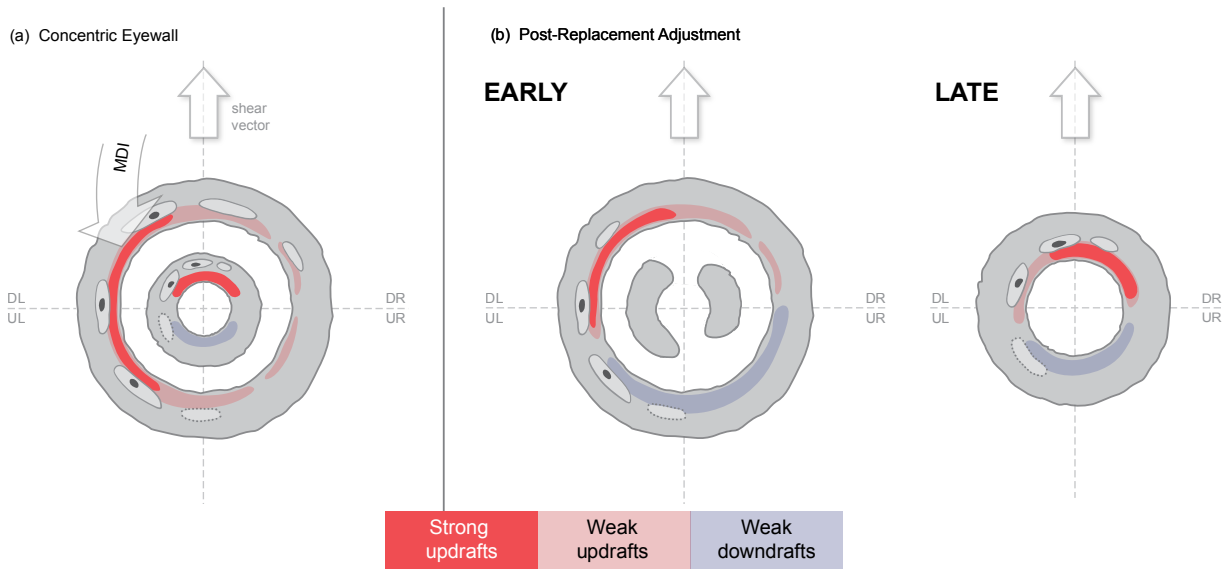
35

FIG. 16. Plan view schematic of eyewall structures analyzed during the two ERC periods: (a) Concentric Eyewall and (b) Post-Replacement Adjustment (Early and Late). Shaded areas represent reflectivity patterns of the eyewall stages. Convective cells of higher reflectivity are embedded within the eyewall rings. Regions of strong updrafts, weak updrafts, and weak downdrafts are also indicated. The environmental wind shear vector points upward and defines the four storm quadrants. The Concentric Eyewall period shows mesoscale descending inflow (MDI) in the DL quadrant. The Early and Late stages of the Post-Replacement Adjustment period show a decaying inner eyewall in the Early time followed by the return to a single eyewall structure in the Late time. Adapted from Didlake et al. (2017) and Didlake et al. (2018).

larger radii and ends along the strongest outer eyewall updrafts and reflectivity. In previous studies, the MDI was found in the stratiform region of the left-of-shear rainband complex (Didlake and Houze 2013; Didlake et al. 2018) and formed by widespread evaporative and melting cooling (Qiu and Tan 2013; Didlake and Houze 2013; Didlake et al. 2018; Yu and Didlake 2019; Yu et al. 2021, 2022; Wang and Tan 2022). Yu and Didlake (2019) and Yu et al. (2022) also showed that when the MDI sunk to the boundary layer as a cold pool of air, warmer boundary layer air from the DR quadrant converged with the cold pool, and new convective updrafts were triggered left-of-shear via buoyancy advection. We hypothesize that the same processes occurred here in Ivan. Since the MDI is largely rainband-driven, we hypothesize that it pre-existed the outer eyewall and its

continuing presence helped force the outer eyewall asymmetry after the eyewall formed (Didlake et al. 2018; Yu et al. 2021, 2022).

The Post-Replacement Adjustment period in Fig. 16b shows the Early and Late stages within this period. The Early stage depicts the outer eyewall with an updraft maximum in the DL quadrant, which produces the reflectivity maximum in the UL quadrant. The outer eyewall updraft maximum in the DL quadrant is consistent with the hypothesis of updraft forcing from collocated MDI processes in the Concentric Eyewall period. The configurations of updraft and precipitation maxima during the Concentric Eyewall and Early Post-Replacement Adjustment are still slightly different; these differences may be due to variability between the two ERC events that are studied. Also illustrated in Fig. 16b in gray is the decaying inner eyewall. The outer eyewall updraft maximum and precipitation maximum both shift anticyclonically upwind in the Late stage of the Post-Replacement Adjustment period, ending with both updraft and reflectivity maxima located in the downshear quadrants. The orientation of the asymmetries during the Concentric Eyewall period and the upwind shift seen at the end of the ERC support the findings of Didlake et al. (2017). It is hypothesized that this upwind shift in the outer eyewall updraft maximum is an adjustment of the asymmetry configuration to match that of a sheared single (or inner) eyewall, i.e., updrafts downshear like that seen in the inner eyewall during the Concentric Eyewall period. It follows that this adjustment would be a result of the asymmetric forcing mechanism transitioning from remnant stratiform rainband dynamics to direct interaction with the environmental shear.

The effects of these asymmetries on Ivan's intensity following the ERC remain unclear. Although both ERCs saw a decrease in intensity at the times of maximum wind transition (Fig. 2), following ERC1 Ivan reintensified 10 kts, yet after ERC2, Ivan did not see a reintensification. With similar sea surface temperatures (SSTs; not shown) and shear magnitudes following both ERCs, neither shear nor SSTs are a clear factor for the difference in post-ERC intensification rates. This suggests internal processes may be contributing to this difference. Nolan et al. (2007) showed that asymmetries fundamentally act to weaken a storm, so perhaps the observed asymmetries in Ivan are acting to counter intensification. Although TC intensity is largely governed by the axisymmetric structure, both during and after ERCs (Sitkowski et al. 2011), a full understanding of intensity requires understanding the effects that ERC asymmetries may also have on intensity.

37

This study provides observational evidence to help further understand the physical mechanisms of ERCs and their impacts on TC evolution. These results also can help improve representation of ERC processes in research and operational models by providing observational comparison cases to validate ERC structure fidelity. Additionally, an understanding of asymmetries during an ERC can potentially lead to improved forecasts of wind and precipitation impact locations in intense TCs.

This case study's scope is limited to one storm and its particular environmental conditions such as SSTs, shear profile and evolution, land interactions, and thermodynamic conditions. As such, more observational studies of eyewall replacements are important in building a more complete understanding of ERCs, their dynamics, and associated asymmetries. Comparisons between periods are also limited, given ERC1 has weaker shear compared to ERC2 (Fig. 2). Furthermore, this study is limited to kinematic and precipitation analyses, as full thermodynamic fields and fully continuous observations are unavailable. Future work of modeling studies capable of varying shear and analyzing thermodynamic fields would further help explain the asymmetries and their evolution during ERCs, and the impact of asymmetries on TC intensity.

Data availability statement. The TDR dataset is available from HRD at https://www.aoml.noaa.gov/ftp/pub/hrd/data/radar/level3/.

References

Abarca, S. F., and M. T. Montgomery, 2015: Are eyewall replacement cycles governed largely by axisymmetric balance dynamics? *Journal of the Atmospheric Sciences*, **72 (1)**, 82 – 87, https://doi.org/10.1175/JAS-D-14-0151.1, URL https://journals.ametsoc.org/view/journals/atsc/72/1/jas-d-14-0151.1.xml.

Ahern, K., R. E. Hart, and M. A. Bourassa, 2021: Asymmetric hurricane boundary layer structure during storm decay. part i: Formation of descending inflow. *Monthly Weather Review*, **149 (11)**, 3851 – 3874, https://doi.org/10.1175/MWR-D-21-0030.1, URL https://journals.ametsoc.org/view/journals/mwre/149/11/MWR-D-21-0030.1.xml.

Ahern, K., R. E. Hart, and M. A. Bourassa, 2022: Asymmetric hurricane boundary layer structure during storm decay. part ii: Secondary eyewall formation. *Monthly Weather Review*, **150 (8)**, 1915 – 1936, https://doi.org/10.1175/MWR-D-21-0247.1, URL https://journals.ametsoc.org/view/journals/mwre/150/8/MWR-D-21-0247.1.xml.

Alvey, G. R., E. Zipser, and J. Zawislak, 2020: How does hurricane edouard (2014) evolve toward symmetry before rapid intensification? a high-resolution ensemble study. *Journal of the Atmospheric Sciences*, **77 (4)**, 1329 – 1351, https://doi.org/https://doi.org/10.1175/JAS-D-18-0355.1, URL https://journals.ametsoc.org/view/journals/atsc/77/4/jas-d-18-0355.1.xml.

Bell, G. D., and Coauthors, 2000: Climate assessment for 1999. *Bulletin of the American Meteorological Society*, **81 (6)**, S1 – S50, https://doi.org/https://doi.org/10.1175/1520-0477(2000)81[s1:CAF]2.0.CO;2, URL https://journals.ametsoc.org/view/journals/bams/81/6/1520-0477_2000_81_s1_caf_2_0_co_2.xml.

Bell, M. M., M. T. Montgomery, and W.-C. Lee, 2012: An axisymmetric view of concentric eyewall evolution in hurricane rita (2005). *Journal of the Atmospheric Sciences*, **69 (8)**, 2414 – 2432, https://doi.org/10.1175/JAS-D-11-0167.1, URL https://journals.ametsoc.org/view/journals/atsc/69/8/jas-d-11-0167.1.xml.

Bender, M. A., 1997: The effect of relative flow on the asymmetric structure in the interior of hurricanes. *Journal of the Atmospheric Sciences*, **54 (6)**, 703–724, https://doi.org/10.1175/1520-0469(1997)054⟨0703:TEORFO⟩2.0.CO;2.

Black, M. L., J. F. Gamache, F. D. Marks, C. E. Samsury, and H. E. Willoughby, 2002: Eastern pacific hurricanes jimena of 1991 and olivia of 1994: The effect of vertical shear on structure and intensity. *Monthly Weather Review*, **130 (9)**, 2291 – 2312, https://doi.org/10.1175/1520-0493(2002)130⟨2291:EPHJOA⟩2.0.CO;2, URL https://journals.ametsoc.org/view/journals/mwre/130/9/1520-0493_2002_130_2291_ephjoa_2.0.co_2.xml.

Black, M. L., and H. E. Willoughby, 1992: The concentric eyewall cycle of hurricane gilbert. *Monthly Weather Review*, **120 (6)**, 947 – 957, https://doi.org/https://doi.org/10.1175/1520-0493(1992)120⟨0947:TCECOH⟩2.0.CO;2, URL https://journals.ametsoc.org/view/journals/mwre/120/6/1520-0493_1992_120_0947_tcecoh_2_0_co_2.xml.

Boehm, A. M., and M. M. Bell, 2021: Retrieved thermodynamic structure of hurricane rita (2005) from airborne multi–doppler radar data. *Journal of the Atmospheric Sciences*, **78 (5)**, 1583 – 1605, https://doi.org/https://doi.org/10.1175/JAS-D-20-0195.1, URL https://journals.ametsoc.org/view/journals/atsc/78/5/JAS-D-20-0195.1.xml.

Braun, S. A., M. T. Montgomery, and Z. Pu, 2006: High-resolution simulation of hurricane bonnie (1998). part i: The organization of eyewall vertical motion. *Journal of the Atmospheric Sciences*, **63 (1)**, 19 – 42, https://doi.org/10.1175/JAS3598.1, URL https://journals.ametsoc.org/view/journals/atsc/63/1/jas3598.1.xml.

Burg, T., and S. Lillo, 2022: Tropycal: A tropical cyclone data and visualization package for python. URL https://github.com/tropycal/tropycal.

Cha, T.-Y., M. M. Bell, and A. J. DesRosiers, 2021: Doppler radar analysis of the eyewall replacement cycle of hurricane matthew (2016) in vertical wind shear. *Monthly Weather Review*, **149 (9)**, 2927 – 2943, https://doi.org/10.1175/MWR-D-20-0289.1, URL https://journals.ametsoc.org/view/journals/mwre/149/9/MWR-D-20-0289.1.xml.

Chen, S. S., J. A. Knaff, and F. D. Marks, 2006: Effects of vertical wind shear and storm motion on tropical cyclone rainfall asymmetries deduced from trmm. *Monthly Weather Review*, **134 (11)**, 3190 – 3208, https://doi.org/10.1175/MWR3245.1, URL https://journals.ametsoc.org/view/journals/mwre/134/11/mwr3245.1.xml.

Cheung, A. A., C. J. Slocum, J. A. Knaff, and M. N. Razin, 2023: Documenting the progressions of secondary eyewall formations. *Weather and Forecasting*, https://doi.org/https://doi.org/10.1175/WAF-D-23-0047.1, URL https://journals.ametsoc.org/view/journals/wefo/aop/WAF-D-23-0047.1/WAF-D-23-0047.1.xml.

Davis, C., C. Snyder, and A. C. Didlake, 2008: A vortex-based perspective of eastern Pacific tropical cyclone formation. *Monthly Weather Review*, **136 (7)**, 2461–2477, https://doi.org/10.1175/2007MWR2317.1.

DeHart, J. C., R. A. Houze, and R. F. Rogers, 2014: Quadrant distribution of tropical cyclone inner-core kinematics in relation to environmental shear. *Journal of the Atmospheric Sciences*, **71 (7)**, 2713 – 2732, https://doi.org/10.1175/JAS-D-13-0298.1, URL https://journals.ametsoc.org/view/journals/atsc/71/7/jas-d-13-0298.1.xml.

DeMaria, M., and J. Kaplan, 1994: A statistical hurricane intensity prediction scheme (ships) for the atlantic basin. *Weather and Forecasting*, **9 (2)**, 209 – 220, https://doi.org/10.1175/1520-0434(1994)009⟨0209:ASHIPS⟩2.0.CO;2, URL https://journals.ametsoc.org/view/journals/wefo/9/2/1520-0434_1994_009_0209_aships_2_0_co_2.xml.

Didlake, A. C., G. M. Heymsfield, P. D. Reasor, and S. R. Guimond, 2017: Concentric eyewall asymmetries in Hurricane Gonzalo (2014) observed by airborne radar. *Monthly Weather Review*, **145 (3)**, 729–749, https://doi.org/10.1175/MWR-D-16-0175.1.

41

Didlake, A. C., and R. A. Houze, 2009: Convective-scale downdrafts in the principal rainband of hurricane Katrina (2005). *Monthly Weather Review*, **137 (10)**, 3269–3293, https://doi.org/10.1175/2009MWR2827.1.

Didlake, A. C., and R. A. Houze, 2013: Dynamics of the Stratiform Sector of a Tropical Cyclone Rainband. *Journal of the Atmospheric Sciences*, **70 (7)**, 1891–1911, https://doi.org/10.1175/JAS-D-12-0245.1.

Didlake, A. C., and M. R. Kumjian, 2018: Examining Storm Asymmetries in Hurricane Irma (2017) Using Polarimetric Radar Observations. *Geophysical Research Letters*, **45 (24)**, 13,513–13,522, https://doi.org/10.1029/2018GL080739.

Didlake, A. C., P. D. Reasor, R. F. Rogers, and W. C. Lee, 2018: Dynamics of the transition from Spiral Rainbands to a secondary eyewall in Hurricane Earl (2010). *Journal of the Atmospheric Sciences*, **75 (9)**, 2909–2929, https://doi.org/10.1175/JAS-D-17-0348.1.

Dodge, P., R. W. Burpee, and F. D. Marks, 1999: The kinematic structure of a hurricane with sea level pressure less than 900 mb. *Monthly Weather Review*, **127 (6)**, 987 – 1004, https://doi.org/https://doi.org/10.1175/1520-0493(1999)127⟨0987:TKSOAH⟩2.0.CO;2, URL https://journals.ametsoc.org/view/journals/mwre/127/6/1520-0493_1999_127_0987_tksoah_2.0.co_2.xml.

Eastin, M. D., W. M. Gray, and P. G. Black, 2005: Buoyancy of convective vertical motions in the inner core of intense hurricanes. part ii: Case studies. *Monthly Weather Review*, **133 (1)**, 209 – 227, https://doi.org/10.1175/MWR-2849.1, URL https://journals.ametsoc.org/view/journals/mwre/133/1/mwr-2849.1.xml.

Fischer, M. S., P. D. Reasor, R. F. Rogers, and J. F. Gamache, 2022: An analysis of tropical cyclone vortex and convective characteristics in relation to storm intensity using a novel airborne doppler radar database. *Monthly Weather Review*, **150 (9)**, 2255 – 2278, https://doi.org/https://doi.org/10.1175/MWR-D-21-0223.1, URL https://journals.ametsoc.org/view/journals/mwre/150/9/MWR-D-21-0223.1.xml.

Fischer, M. S., R. F. Rogers, and P. D. Reasor, 2020: The rapid intensification and eyewall replacement cycles of hurricane irma (2017). *Monthly Weather Review*, **148 (3)**, 981

– 1004, https://doi.org/10.1175/MWR-D-19-0185.1, URL https://journals.ametsoc.org/view/journals/mwre/148/3/mwr-d-19-0185.1.xml.

Foerster, A. M., and M. M. Bell, 2017: Thermodynamic retrieval in rapidly rotating vortices from multiple-doppler radar data. *Journal of Atmospheric and Oceanic Technology*, **34 (11)**, 2353 – 2374, https://doi.org/10.1175/JTECH-D-17-0073.1, URL https://journals.ametsoc.org/view/journals/atot/34/11/jtech-d-17-0073.1.xml.

Frank, W. M., and E. A. Ritchie, 1999: Effects of environmental flow upon tropical cyclone structure. *Monthly Weather Review*, **127 (9)**, 2044–2061, https://doi.org/10.1175/1520-0493(1999)127⟨2044:EOEFUT⟩2.0.CO;2.

Frank, W. M., and E. A. Ritchie, 2001: Effects of vertical wind shear on the intensity and structure of numerically simulated hurricanes. *Monthly Weather Review*, **129 (9)**, 2249–2269, https://doi.org/10.1175/1520-0493(2001)129⟨2249:EOVWSO⟩2.0.CO;2.

Gamache, J. F., 1997: Evaluation of a fully three-dimensional vari- ational Doppler analysis technique. *28th Conf. on Radar Meteorology*.

Gao, J., M. Xue, A. Shapiro, and K. K. Droegemeier, 1999: A variational method for the analysis of three-dimensional wind fields from two Doppler radars. *Monthly Weather Review*, **127 (9)**, 2128–2142, https://doi.org/10.1175/1520-0493(1999)127⟨2128:AVMFTA⟩2.0.CO;2.

Guimond, S. R., P. D. Reasor, G. M. Heymsfield, and M. M. McLinden, 2020: The dynamics of vortex rossby waves and secondary eyewall development in hurricane matthew (2016): New insights from radar measurements. *Journal of the Atmospheric Sciences*, **77 (7)**, 2349 – 2374, https://doi.org/10.1175/JAS-D-19-0284.1, URL https://journals.ametsoc.org/view/journals/atsc/77/7/jasD190284.xml.

Hazelton, A. T., and R. E. Hart, 2013: Hurricane eyewall slope as determined from airborne radar reflectivity data: Composites and case studies. *Weather and Forecasting*, **28 (2)**, 368 – 386, https://doi.org/https://doi.org/10.1175/WAF-D-12-00037.1, URL https://journals.ametsoc.org/view/journals/wefo/28/2/waf-d-12-00037_1.xml.

Hazelton, A. T., R. Rogers, and R. E. Hart, 2015: Shear-relative asymmetries in tropical cyclone eyewall slope. *Monthly Weather Review*, **143 (3)**, 883 – 903, https://doi.org/

10.1175/MWR-D-14-00122.1, URL https://journals.ametsoc.org/view/journals/mwre/143/3/mwr-d-14-00122.1.xml.

Hence, D. A., and R. A. Houze, 2011: Vertical structure of hurricane eyewalls as seen by the trmm precipitation radar. *Journal of the Atmospheric Sciences*, **68 (8)**, 1637 – 1652, https://doi.org/10.1175/2011JAS3578.1, URL https://journals.ametsoc.org/view/journals/atsc/68/8/2011jas3578.1.xml.

Hence, D. A., and R. A. Houze, 2012: Vertical structure of tropical cyclones with concentric eyewalls as seen by the TRMM precipitation radar. *Journal of the Atmospheric Sciences*, **69 (3)**, 1021–1036, https://doi.org/10.1175/JAS-D-11-0119.1.

Homeyer, C. R., and Coauthors, 2021: Polarimetric signatures in landfalling tropical cyclones. *Monthly Weather Review*, **149 (1)**, 131 – 154, https://doi.org/10.1175/MWR-D-20-0111.1, URL https://journals.ametsoc.org/view/journals/mwre/149/1/mwr-d-20-0111.1.xml.

Houze, R. A., S. S. Chen, B. F. Smull, W.-C. Lee, and M. M. Bell, 2007: Hurricane intensity and eyewall replacement. *Science*, **315 (5816)**, 1235–1239, https://doi.org/10.1126/science.1135650, URL https://www.science.org/doi/abs/10.1126/science.1135650, https://www.science.org/doi/pdf/10.1126/science.1135650.

Huang, Y.-H., M. T. Montgomery, and C.-C. Wu, 2012: Concentric eyewall formation in typhoon sinlaku (2008). part ii: Axisymmetric dynamical processes. *Journal of the Atmospheric Sciences*, **69 (2)**, 662 – 674, https://doi.org/10.1175/JAS-D-11-0114.1, URL https://journals.ametsoc.org/view/journals/atsc/69/2/jas-d-11-0114.1.xml.

Jones, S. C., 1995: The evolution of vortices in vertical shear. I: Initially barotropic vortices. *Quarterly Journal of the Royal Meteorological Society*, **121 (524)**, 821–851, https://doi.org/10.1002/qj.49712152406.

Jorgensen, D. P., T. J. Matejka, and J. D. DuGranrut, 1996: Multi-beam techniques for deriving wind fields from airborne doppler radars. *Meteorology and Atmospheric Physics*, **59**, 83–104.

Judt, F., and S. S. Chen, 2010: Convectively generated potential vorticity in rainbands and formation of the secondary eyewall in Hurricane Rita of 2005. *Journal of the Atmospheric Sciences*, **67 (11)**, 3581–3599, https://doi.org/10.1175/2010JAS3471.1.

44

Kepert, J. D., 2013: How does the boundary layer contribute to eyewall replacement cycles in axisymmetric tropical cyclones? *Journal of the Atmospheric Sciences*, **70 (9)**, 2808 – 2830, https://doi.org/10.1175/JAS-D-13-046.1, URL https://journals.ametsoc.org/view/journals/atsc/70/9/jas-d-13-046.1.xml.

Marks, F. D., and R. A. Houze, 1987: Inner core structure of hurricane alicia from airborne doppler radar observations. *J. Atmos. Sci.*, **44**, 1296–1317.

Molinari, J., and D. Vollaro, 2014: Symmetric instability in the outflow layer of a major hurricane. *Journal of the Atmospheric Sciences*, **71 (10)**, 3739 – 3746, https://doi.org/10.1175/JAS-D-14-0117.1, URL https://journals.ametsoc.org/view/journals/atsc/71/10/jas-d-14-0117.1.xml.

Molinari, J., J. A. Zhang, R. F. Rogers, and D. Vollaro, 2019: Repeated eyewall replacement cycles in hurricane frances (2004). *Monthly Weather Review*, **147 (6)**, 2009 – 2022, https://doi.org/https://doi.org/10.1175/MWR-D-18-0345.1, URL https://journals.ametsoc.org/view/journals/mwre/147/6/mwr-d-18-0345.1.xml.

Montgomery, M. T., and J. Persing, 2021: Does balance dynamics well capture the secondary circulation and spinup of a simulated hurricane? *Journal of the Atmospheric Sciences*, **78 (1)**, 75 – 95, https://doi.org/10.1175/JAS-D-19-0258.1, URL https://journals.ametsoc.org/view/journals/atsc/78/1/jas-d-19-0258.1.xml.

Nguyen, L. T., R. Rogers, J. Zawislak, and J. A. Zhang, 2019: Assessing the influence of convective downdrafts and surface enthalpy fluxes on tropical cyclone intensity change in moderate vertical wind shear. *Monthly Weather Review*, **147 (10)**, 3519 – 3534, https://doi.org/https://doi.org/10.1175/MWR-D-18-0461.1, URL https://journals.ametsoc.org/view/journals/mwre/147/10/mwr-d-18-0461.1.xml.

Nolan, D. S., Y. Moon, and D. P. Stern, 2007: Tropical cyclone intensification from asymmetric convection: Energetics and efficiency. *Journal of the Atmospheric Sciences*, **64 (10)**, 3377 – 3405, https://doi.org/https://doi.org/10.1175/JAS3988.1, URL https://journals.ametsoc.org/view/journals/atsc/64/10/jas3988.1.xml.

Persing, J., and M. T. Montgomery, 2022: Does the rotating convection paradigm describe secondary eyewall formation in idealized three-dimensional simulations? *Journal of the Atmospheric Sciences*, **79 (3)**, 745 – 762, https://doi.org/10.1175/JAS-D-21-0143.1, URL https://journals.ametsoc.org/view/journals/atsc/79/3/JAS-D-21-0143.1.xml.

Qin, N., L. Wu, and Q. Liu, 2021: Evolution of the moat associated with the secondary eyewall formation in a simulated tropical cyclone. *Journal of the Atmospheric Sciences*, **78 (12)**, 4021 – 4035, https://doi.org/10.1175/JAS-D-20-0375.1, URL https://journals.ametsoc.org/view/journals/atsc/78/12/JAS-D-20-0375.1.xml.

Qiu, X., and Z.-M. Tan, 2013: The roles of asymmetric inflow forcing induced by outer rainbands in tropical cyclone secondary eyewall formation. *Journal of the Atmospheric Sciences*, **70 (3)**, 953 – 974, https://doi.org/10.1175/JAS-D-12-084.1, URL https://journals.ametsoc.org/view/journals/atsc/70/3/jas-d-12-084.1.xml.

Razin, M. N., and M. M. Bell, 2021: The unconventional eyewall replacement cycle of hurricane ophelia (2005). *Monthly Weather Review*, **149 (7)**, 2151 – 2170, https://doi.org/10.1175/MWR-D-20-0181.1, URL https://journals.ametsoc.org/view/journals/mwre/149/7/MWR-D-20-0181.1.xml.

Reasor, P. D., and M. D. Eastin, 2012: Rapidly intensifying hurricane guillermo (1997). part ii: Resilience in shear. *Monthly Weather Review*, **140 (2)**, 425 – 444, https://doi.org/https://doi.org/10.1175/MWR-D-11-00080.1, URL https://journals.ametsoc.org/view/journals/mwre/140/2/mwr-d-11-00080.1.xml.

Reasor, P. D., M. D. Eastin, and J. F. Gamache, 2009: Rapidly intensifying hurricane Guillermo (1997). Part I: Low-wavenumber structure and evolution. *Monthly Weather Review*, **137 (2)**, 603–631, https://doi.org/10.1175/2008MWR2487.1.

Reasor, P. D., M. T. Montgomery, and L. D. Grasso, 2004: A new look at the problem of tropical cyclones in vertical shear flow: Vortex resiliency. *Journal of the Atmospheric Sciences*, **61 (1)**, 3–22, https://doi.org/10.1175/1520-0469(2004)061⟨0003:ANLATP⟩2.0.CO;2.

Reasor, P. D., M. T. Montgomery, F. D. Marks, and J. F. Gamache, 2000: Low-wavenumber structure and evolution of the hurricane inner core observed by airborne dual-doppler radar. *Monthly*

Weather Review, **128 (6)**, 1653 – 1680, https://doi.org/https://doi.org/10.1175/1520-0493(2000) 128⟨1653:LWSAEO⟩2.0.CO;2, URL https://journals.ametsoc.org/view/journals/mwre/128/6/ 1520-0493_2000_128_1653_lwsaeo_2.0.co_2.xml.

Reasor, P. D., R. Rogers, and S. Lorsolo, 2013: Environmental flow impacts on tropical cyclone structure diagnosed from airborne doppler radar composites. *Monthly Weather Review*, **141 (9)**, 2949–2969, https://doi.org/10.1175/MWR-D-12-00334.1.

Riemer, M., M. T. Montgomery, and M. E. Nicholls, 2010: A new paradigm for intensity modification of tropical cyclones: thermodynamic impact of vertical wind shear on the inflow layer. *Atmospheric Chemistry and Physics*, **10 (7)**, 3163–3188, https://doi.org/10.5194/acp-10-3163-2010, URL https://acp.copernicus.org/articles/10/3163/2010/.

Riemer, M., M. T. Montgomery, and M. E. Nicholls, 2013: Further examination of the thermodynamic modification of the inflow layer of tropical cyclones by vertical wind shear. *Atmospheric Chemistry and Physics*, **13 (1)**, 327–346, https://doi.org/10.5194/acp-13-327-2013, URL https://acp.copernicus.org/articles/13/327/2013/.

Rogers, R., S. Lorsolo, P. Reasor, J. Gamache, and F. Marks, 2012: Multiscale analysis of tropical cyclone kinematic structure from airborne doppler radar composites. *Monthly Weather Review*, **140 (1)**, 77–99, https://doi.org/10.1175/MWR-D-10-05075.1.

Rogers, R., P. Reasor, and S. Lorsolo, 2013: Airborne doppler observations of the inner-core structural differences between intensifying and steady-state tropical cyclones. *Monthly Weather Review*, **141 (9)**, 2970–2991, https://doi.org/10.1175/MWR-D-12-00357.1.

Rozoff, C. M., W. H. Schubert, and J. P. Kossin, 2008: Some dynamical aspects of tropical cyclone concentric eyewalls. *Quarterly Journal of the Royal Meteorological Society*, **134 (632)**, 583–593, https://doi.org/https://doi.org/10.1002/qj.237, URL https://rmets.onlinelibrary.wiley.com/ doi/abs/10.1002/qj.237, https://rmets.onlinelibrary.wiley.com/doi/pdf/10.1002/qj.237.

Rozoff, C. M., W. H. Schubert, B. D. McNoldy, and J. P. Kossin, 2006: Rapid filamentation zones in intense tropical cyclones. *Journal of the Atmospheric Sciences*, **63 (1)**, 325–340, https://doi.org/10.1175/JAS3595.1.

Samsury, C. E., and E. J. Zipser, 1995: Secondary Wind Maxima in Hurricanes: Airflow and Relationship to Rainbands. *Monthly Weather Review*, **123 (12)**, 3502–3517, https://doi.org/10.1175/1520-0493(1995)123\%3C3502:SWMIHA\%3E2.0.CO;2.

Shapiro, L. J., and H. E. Willoughby, 1982: The response of balanced hurricanes to local sources of heat and momentum. *Journal of the Atmospheric Sciences*, **39 (2)**, 378–394, https://doi.org/10.1175/1520-0469(1982)039⟨0378:TROBHT⟩2.0.CO;2.

Shimada, U., M. Sawada, and H. Yamada, 2018: Doppler radar analysis of the rapid intensification of typhoon goni (2015) after eyewall replacement. *Journal of the Atmospheric Sciences*, **75 (1)**, 143 – 162, https://doi.org/10.1175/JAS-D-17-0042.1, URL https://journals.ametsoc.org/view/journals/atsc/75/1/jas-d-17-0042.1.xml.

Sitkowski, M., J. P. Kossin, and C. M. Rozoff, 2011: Intensity and structure changes during hurricane eyewall replacement cycles. *Monthly Weather Review*, **139 (12)**, 3829 – 3847, https://doi.org/10.1175/MWR-D-11-00034.1, URL https://journals.ametsoc.org/view/journals/mwre/139/12/mwr-d-11-00034.1.xml.

Sitkowski, M., J. P. Kossin, C. M. Rozoff, and J. A. Knaff, 2012: Hurricane eyewall replacement cycle thermodynamics and the relict inner eyewall circulation. *Monthly Weather Review*, **140 (12)**, 4035 – 4045, https://doi.org/10.1175/MWR-D-11-00349.1, URL https://journals.ametsoc.org/view/journals/mwre/140/12/mwr-d-11-00349.1.xml.

Stern, D. P., and D. S. Nolan, 2009: Reexamining the vertical structure of tangential winds in tropical cyclones: Observations and theory. *Journal of the Atmospheric Sciences*, **66 (12)**, 3579 – 3600, https://doi.org/https://doi.org/10.1175/2009JAS2916.1, URL https://journals.ametsoc.org/view/journals/atsc/66/12/2009jas2916.1.xml.

Stevenson, S. N., K. L. Corbosiero, and J. Molinari, 2014: The convective evolution and rapid intensification of hurricane earl (2010). *Monthly Weather Review*, **142 (11)**, 4364 – 4380, https://doi.org/https://doi.org/10.1175/MWR-D-14-00078.1, URL https://journals.ametsoc.org/view/journals/mwre/142/11/mwr-d-14-00078.1.xml.

Stewart, S. R., 2004: Tropical cyclone report hurricane ivan (2004). 1–44, https://doi.org/https://doi.org/10.1175/1520-0469(1987)044⟨0542:AAITFT⟩2.0.CO;2, URL https://www.nhc.noaa.gov/data/tcr/AL092004_Ivan.pdf.

Vaughan, A., K. J. E. Walsh, and J. D. Kepert, 2020: The stationary banding complex and secondary eyewall formation in tropical cyclones. *Journal of Geophysical Research: Atmospheres*, **125 (6)**, e2019JD031 515, https://doi.org/https://doi.org/10.1029/2019JD031515, URL https://agupubs.onlinelibrary.wiley.com/doi/abs/10.1029/2019JD031515, e2019JD031515 10.1029/2019JD031515, https://agupubs.onlinelibrary.wiley.com/doi/pdf/10.1029/2019JD031515.

Vigh, J. L., and Coauthors, 2020: Flight+: The extended flight level dataset for tropical cyclones (version 1.3). https://doi.org/10.5065/D6WS8R93.

Wang, H., Y. Wang, J. Xu, and Y. Duan, 2019: The axisymmetric and asymmetric aspects of the secondary eyewall formation in a numerically simulated tropical cyclone under idealized conditions on an f plane. *Journal of the Atmospheric Sciences*, **76 (1)**, 357 – 378, https://doi.org/10.1175/JAS-D-18-0130.1, URL https://journals.ametsoc.org/view/journals/atsc/76/1/jas-d-18-0130.1.xml.

Wang, Y.-F., and Z.-M. Tan, 2022: Essential dynamics of the vertical wind shear affecting the secondary eyewall formation in tropical cyclones. *Journal of the Atmospheric Sciences*, **79 (11)**, 2831 – 2847, https://doi.org/https://doi.org/10.1175/JAS-D-21-0340.1, URL https://journals.ametsoc.org/view/journals/atsc/79/11/JAS-D-21-0340.1.xml.

Willoughby, H. E., and M. B. Chelmow, 1982: Objective Determination of Hurricane Tracks from Aircraft Observations. *Monthly Weather Review*, **110 (9)**, 1298–1305, https://doi.org/10.1175/1520-0493(1982)110⟨1298:odohtf⟩2.0.co;2.

Willoughby, H. E., J. A. Clos, and M. G. Shoreibah, 1982: Concentric Eye Walls, Secondary Wind Maxima, and The Evolution of the Hurricane Vortex. *Journal of the Atmospheric Sciences*, **39 (2)**, 395–411, https://doi.org/10.1175/1520-0469(1982)039\%3C0395:CEWSWM\%3E2.0.CO;2.

Wunsch, K. E. D., and A. C. Didlake, 2018: Analyzing tropical cyclone structures during secondary eyewall formation using aircraft in situ observations. *Monthly Weather Review*, **146 (12)**,

3977 – 3993, https://doi.org/10.1175/MWR-D-18-0197.1, URL https://journals.ametsoc.org/view/journals/mwre/146/12/mwr-d-18-0197.1.xml.

Yu, C. L., and A. C. Didlake, 2019: Impact of stratiform rainband heating on the tropical cyclone wind field in idealized simulations. *Journal of the Atmospheric Sciences*, **76 (8)**, 2443–2462, https://doi.org/10.1175/JAS-D-18-0335.1.

Yu, C.-L., A. C. Didlake, and F. Zhang, 2022: Updraft maintenance and axisymmetrization during secondary eyewall formation in a model simulation of hurricane matthew (2016). *Journal of the Atmospheric Sciences*, **79 (4)**, 1105 – 1125, https://doi.org/10.1175/JAS-D-21-0103.1, URL https://journals.ametsoc.org/view/journals/atsc/79/4/JAS-D-21-0103.1.xml.

Yu, C.-L., A. C. Didlake, F. Zhang, and R. G. Nystrom, 2021: Asymmetric rainband processes leading to secondary eyewall formation in a model simulation of hurricane matthew (2016). *Journal of the Atmospheric Sciences*, **78 (1)**, 29 – 49, https://doi.org/10.1175/JAS-D-20-0061.1, URL https://journals.ametsoc.org/view/journals/atsc/78/1/jas-d-20-0061.1.xml.

Yuter, S. E., and R. A. Houze, 1995: Three-dimensional kinematic and microphysical evolution of florida cumulonimbus. part ii: Frequency distributions of vertical velocity, reflectivity, and differential reflectivity. *Monthly Weather Review*, **123 (7)**, 1941 – 1963, https://doi.org/10.1175/1520-0493(1995)123⟨1941:TDKAME⟩2.0.CO;2, URL https://journals.ametsoc.org/view/journals/mwre/123/7/1520-0493_1995_123_1941_tdkame_2_0_co_2.xml.

Zhang, F., D. Tao, Y. Q. Sun, and J. D. Kepert, 2017: Dynamics and predictability of secondary eyewall formation in sheared tropical cyclones. *Journal of Advances in Modeling Earth Systems*, **9 (1)**, 89–112, https://doi.org/https://doi.org/10.1002/2016MS000729, URL https://agupubs.onlinelibrary.wiley.com/doi/abs/10.1002/2016MS000729, https://agupubs.onlinelibrary.wiley.com/doi/pdf/10.1002/2016MS000729.

Zhang, J. A., R. F. Rogers, P. D. Reasor, E. W. Uhlhorn, and F. D. Marks, 2013: Asymmetric hurricane boundary layer structure from dropsonde composites in relation to the environmental vertical wind shear. *Monthly Weather Review*, **141 (11)**, 3968–3984, https://doi.org/10.1175/MWR-D-12-00335.1.

Zhu, X.-S., H. Yu, and Y. Wang, 2022: Downwind development in a stationary band complex leading to the secondary eyewall formation in the simulated typhoon soudelor (2015). *Monthly Weather Review*, **150 (10)**, 2459 – 2483, https://doi.org/https://doi.org/10.1175/MWR-D-21-0318.1, URL https://journals.ametsoc.org/view/journals/mwre/150/10/MWR-D-21-0318.1.xml.

Zipser, E. J., 1977: Mesoscale and convective–scale downdrafts as distinct components of squall-line structure. *Monthly Weather Review*, **105 (12)**, 1568 – 1589, https://doi.org/https://doi.org/10.1175/1520-0493(1977)105⟨1568:MACDAD⟩2.0.CO;2, URL https://journals.ametsoc.org/view/journals/mwre/105/12/1520-0493_1977_105_1568_macdad_2_0_co_2.xml.